ACSNANO

www.acsnano.org

ARTICLE

Strengthening Engineered Nanocrystal Three-Dimensional Superlattices via Ligand Conformation and Reactivity

Alexander Plunkett, Michael Kampferbeck, Büsra Bor, Uta Sazama, Tobias Krekeler, Lieven Bekaert, Heshmat Noei, Diletta Giuntini, Michael Fröba, Andreas Stierle, Horst Weller, Tobias Vossmeyer, Gerold A. Schneider,* and Berta Domènech*

Cite This: *ACS Nano* 2022, 16, 11692–11707

Read Online

ACCESS | Metrics & More | Article Recommendations | Supporting Information

ABSTRACT: Nanocrystal assembly into ordered structures provides mesostructural functional materials with a precise control that starts at the atomic scale. However, the lack of understanding on the self-assembly itself plus the poor structural integrity of the resulting supercrystalline materials still limits their application into engineered materials and devices. Surface functionalization of the nanobuilding blocks with organic ligands can be used not only as a means to control the interparticle interactions during self-assembly but also as a reactive platform to further strengthen the final material via ligand cross-linking. Here, we explore the influence of the ligands on superlattice formation and during cross-linking via thermal annealing. We elucidate the effect of the surface functionalization on the nanostructure during self-assembly and show how the ligand-promoted superlattice changes subsequently alter the cross-linking behavior. By gaining further insights on the chemical species derived from the thermally activated cross-linking and its effect in the overall mechanical response, we identify an oxidative radical polymerization as the main mechanism responsible for the ligand cross-linking. In the cascade of reactions occurring during the surface-ligands polymerization, the nanocrystal core material plays a catalytic role, being strongly affected by the anchoring group of the surface ligands. Ultimately, we demonstrate how the found mechanistic insights can be used to adjust the mechanical and nanostructural properties of the obtained nanocomposites. These results enable engineering supercrystalline nanocomposites with improved cohesion while preserving their characteristic nanostructure, which is required to achieve the collective properties for broad functional applications.

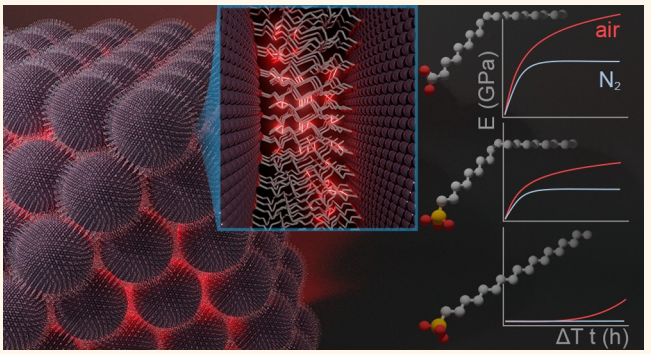

KEYWORDS: *cross-linking, self-assembly, supercrystals, nanocrystals, organic ligands, nanoindentation, robustness*

The periodic arrangement of nanobuilding blocks into singular architectures, reminiscent of atoms in a crystal lattice, allows mesostructural collective phenomena to arise while maintaining the inherent nanocrystal (NC) size-dependent properties.[1−3] By adjusting the building-block materials, size, and shape or their assembling conditions, the collective phenomena can be greatly modified and enhanced. The possibilities are endless, and foreseen applications ranging from mechanics, optics, to electronics, to name a few, emerge.[4−11] However, the lack of structural integrity of these nanoarchitected materials, especially when the material's dimensions are upscaled, still limits their development into industrial materials or their further implementation into functional devices.[1] A promising strategy to overcome this issue is inspired by nature. Nature has evolved hard, strong, and tough materials like bone, teeth, and nacre by hierarchically structuring nanobuilding blocks with thin, soft interphases.[12] Taking inspiration from nature, when NCs are surface-functionalized with organic ligands (NC@ligand) and subsequently arranged into periodic architectures, confined interfacing organic ligands can be cross-linked to boost the

Received: February 8, 2022
Accepted: June 2, 2022
Published: June 27, 2022

https://doi.org/10.1021/acsnano.2c01332
ACS Nano 2022, 16, 11692–11707

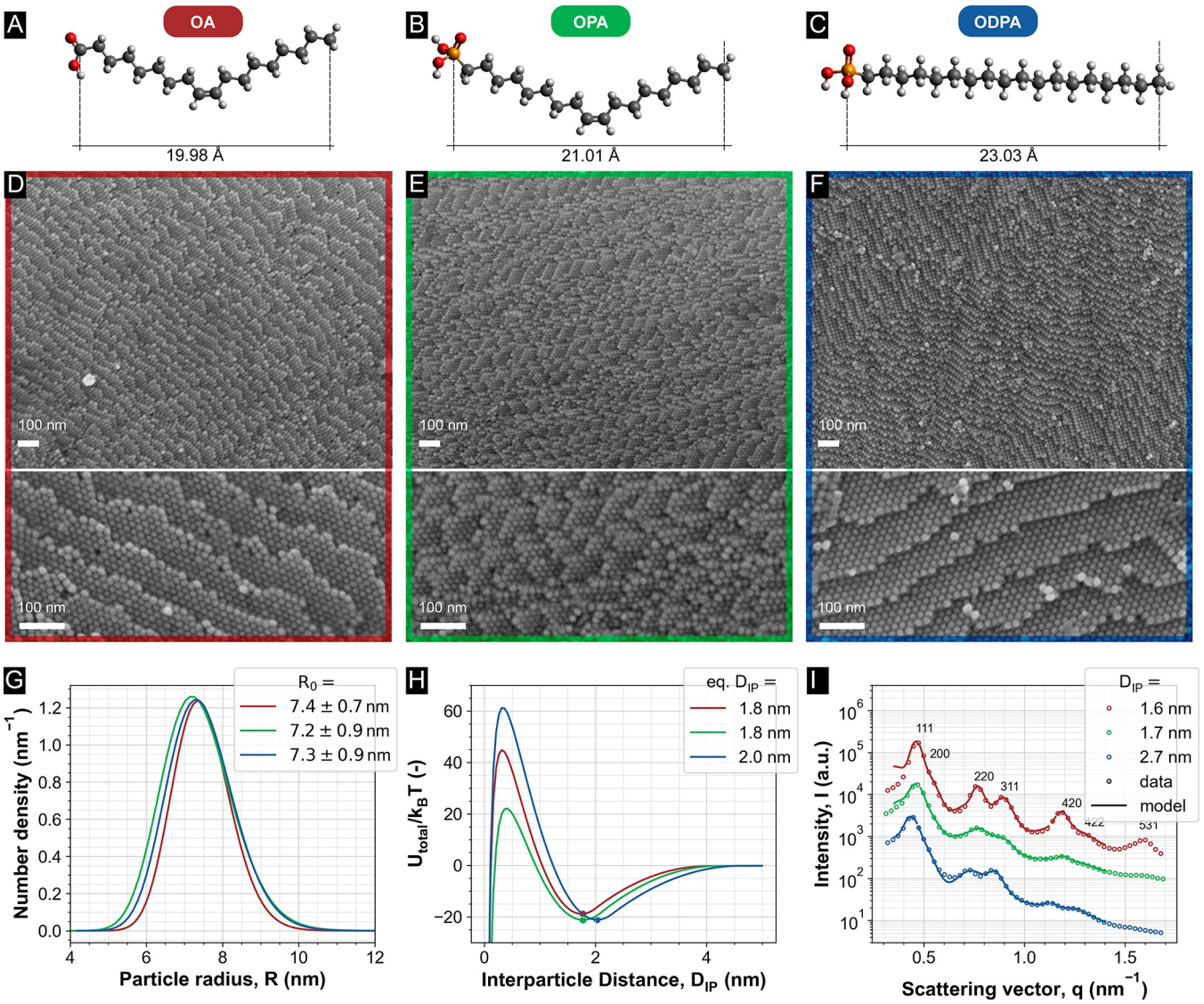

Figure 1. (A–C) Chemical structure and length of the used ligands in the conformation of minimum energy.[43] (D–F) SEM micrographs of cross sections of as-assembled materials. (G) NC core radii (R_0) distribution obtained via SAXS. (H) Calculated particle–particle interactions for each system with the corresponding equilibrium interparticle distances (eq. D_{IP}). (I) SAXS diffraction patterns with FCC indexed peaks for the as-assembled materials and the corresponding interparticle distances, D_{IP}. Color schemes are according to Fe_3O_4@OA, Fe_3O_4@OPA, and Fe_3O_4@ODPA (defined in (A–C)), as red, green, and blue, respectively.

robustness of supercrystalline (SC) materials. It has recently been shown how annealing self-assembled organo-functionalized NCs at moderate temperatures (ca. 350 °C) allows a materials' enhancement of strength, hardness, and stiffness, while still maintaining a high degree of fracture toughness and functionality.[4,5,7,13−17]

In fact, surface ligands are an asset not only for improved material cohesion but also for fine-tuned superlattice formation and for the final material's functionality and applications. One key parameter that can be tuned by the ligands is the interparticle distance between neighboring NCs, where small changes can significantly alter the SC collective properties and therefore change their, for example, plasmonic, conductive, or magnetic behavior. The choice of the ligands and the understanding of their reactivity become crucial factors during materials development.[2,18]

Despite the myriad of ligand possibilities available, in practice a rather limited number of molecules are used; special emphasis being put on aliphatic-derived species, with anchoring groups chosen depending on the NC core surface chemistry.[18] These are versatile systems during NC nucleation and growth and in some instances even rely on naturally occurring molecules (e.g., fatty acids or organophosphates). The specific role played by the organic ligands is, however, complex. Factors such as the grafting density and grafting modes or interfacing position, conformation, and organization on NC surfaces are experimentally challenging to control and measure. Therefore, their implications during superlattice formation or in the final material's properties are not yet unambiguously resolved.[4,14,19−27] Recent research has nevertheless greatly expanded the knowledge of the role played by the ligands' aliphatic chain during self-assembly, highlighting the importance of the ligand shell in mediating superlattice's formation.[14,19,20,25,27−30] Moreover, several studies are also shedding light on the influence of the ligands' functional group. It is emerging that the surface-coordinated species affect: (i)

https://doi.org/10.1021/acsnano.2c01332
ACS Nano 2022, 16, 11692−11707

the NC surface, contributing to the overall electronic structure, promoting near-surface restructuring events;[18,31,32] (ii) the conformation and position of the ligand molecules on the surface, thus affecting the overall NC organic shell;[33−36] (iii) the stability of the functionalization;[18,37,38] and (iv) the overall reactivity of the NC@ligand.[39] How these NC@ligand specific aspects ultimately impact the SC formation and the final system reactivity, especially when the ligands are used as reactive platforms, is yet to be elucidated. A systematic study on the ligand's characteristics (aliphatic chain and anchoring group) is therefore required to disentangle the multifold influences of the surface ligands in SC materials.

Based on the use of monodisperse magnetite (Fe_3O_4) NC cores with different surface functionalization, we investigate the effect of different ligands in evaporative self-assembly. We further show the importance of understanding the reactivity of each NC@ligand system when these are used as cross-linking platforms.

Three surface ligands are explored, selected based on two variables: their aliphatic chain and their anchoring group to the NC surface. For the first, all selected ligands contain the same number of carbons (C18), but either a more reactive double C═C bond in the C9 position or none. The anchoring groups are chosen based on their affinity to the magnetite core, being either carboxylate ($R-COO^-$) or phosphonate ($R-PO_3^{2-}$).[40−42] We show how small differences in the colloidal stability and the presence or absence of a C═C bond have significant effects in the SCs' formation. After exploring the influence of each ligand system in the nanoarchitecture, we further take advantage of a strengthening strategy by ligand cross-linking, which is thermally activated.[7,13,14] Although the ligands' behavior with increasing temperatures is a critical step to not only gain material's robustness by cross-linking but also avoid detriment of functionality by full organic decomposition,[13,16] the exact mechanism of this step and its effects on the ligand shell are yet to be elucidated. We show how the cross-linking reaction relies not only on the specific ligands' reactivity but also on their anchoring to the NC core, which plays a catalytic role.

Unravelling the role played by the ligands in both the formation and reactivity of the superlattices allows us to rationally tailor the mechanical properties of the final three-dimensional (3D) SC materials, a necessary step toward bridging the molecular and the macroscopic length scales in SC materials.

RESULTS AND DISCUSSION

Effect of the Ligands on Self-Assembly. Spherical magnetite (Fe_3O_4) NCs with narrow size distributions (Figure S1) were surface functionalized with three different ligands: oleic acid (OA, $C_{17}H_{33}COOH$), oleyl phosphonic acid (OPA, $C_{18}H_{35}PO(OH)_2$), or octadecyl phosphonic acid (ODPA, $C_{18}H_{37}PO(OH)_2$). As depicted in Figure 1A,B, OA and OPA have a similar aliphatic chain with one C═C double bond (at C9) and differ by the anchoring group to the NC surface: either a carboxylate or a phosphonate for OA and OPA, respectively. The ODPA ligand contains the same binding group as OPA, but with a saturated C18 aliphatic chain (Figure 1C). Aiming for a systematic comparison of the ligands and their possible effects during self-assembly and when used as a reactive platforms, the size and size dispersion of the spherical NC magnetite cores were maintained practically constant between systems (Figure 1, ca. 2.7% and 24% difference in mean size and standard deviations, respectively). For the three systems, the ligand grafting density (ν, number of ligand molecules per NC surface area measured via elemental analysis (EA)) was close to the maximum amount required to obtain a ligand monolayer on the corresponding NC cores (SI Section 1.2 and Table S1). Fe_3O_4@OA, Fe_3O_4@OPA, and Fe_3O_4@ODPA suspensions in toluene were self-assembled under controlled evaporation at ambient conditions. More information about the NCs surface modifications, characterization, and further self-assembly can be found in the Experimental Section.

We first studied the stability of the different ligand-coated NCs in suspension based on particle−particle interactions via an extension of the colloid theory which combines the classical Derjaguin−Landau−Verwey−Overbeek theory[44,45] with the Flory−Huggins model.[46,47] Similar to previous studies,[48−52] we combined the van der Waals' expression for the NC-cores attraction with ligand−ligand and ligand−solvent interactions. Further details are provided in the SI Section 1.3.

It is important to mention that this model oversimplifies the real situation. Intermolecular interactions between surface-functionalized NCs are also influenced by parameters such as the structure of the solvent,[30,53] the structure of the ligand shell,[28−56] or possible sorption−desorption processes of the surface ligands.[14,19,55,57] Nevertheless, to date this is the best available analytical model that does not require, for example, molecular dynamic simulations, and for the purposes of the current study, it assists in predicting the effect of the different ligands on the overall colloidal stability. As per the developed model, under the studied conditions, the interactions are attractive at interparticle distances (D_{IP}, distance between NC core surfaces) between 1.7 ± 0.2 nm and 4.0 ± 0.2 nm for the calculated ligand lengths, l, mainly due to the rather low solvation of the ligand shells in toluene (the calculated Flory parameter falls slightly above 0.5, indicating that the free energy of mixing of solvent and ligands is slightly positive). The energy of the local minima decreases (i.e., the interaction forces become more attractive) with increasing grafting density and molecular volume of the ligands, while increasing the ligand length has the opposite effect (as shown in eqs 10−15 in SI Section 1.3). At $D_{IP} < l$, a strong repulsion due to the elastic contribution arises. For the studied systems, the overall colloidal stability is comparable, but a slight trend arises (from more to less stable): Fe_3O_4@OA > Fe_3O_4@ODPA > Fe_3O_4@OPA (Figure 1H).

The scanning electron microscopy (SEM) evaluation of fracture surfaces of the materials obtained reveals that, for all the starting suspensions used, the self-assembly resulted in ordered arrangements of NCs, with μm-sized SC domains (Figure 1D−F). Due to long-range Bragg reflections arising in the small-angle X-ray scattering (SAXS) signal for highly ordered particles, SAXS was used to further characterize the SC structures. As described in the SI Section 2.1, for all samples the relative peak positions, q_i, corresponding to lattice planes (hkl), are consistent with a face-centered-cubic (FCC) structure (with $q_i/q_{111} = \sqrt{(h^2 + k^2 + l^2)/3}$). The appearance of Debye−Sherrer rings (Figure S5) confirms an isotropic polycrystalline structure, as expected due to the macro-dimensions of the specimens (cm-scale). Moreover, SAXS diffraction patterns of the different SC materials indicate that the quality of the order, as portrayed by the splitting of the (220) and (311) peaks, follows the same trend as the stability prediction (Figure 1D). The sharpness of the SAXS diffraction

https://doi.org/10.1021/acsnano.2c01332
ACS Nano 2022, 16, 11692−11707

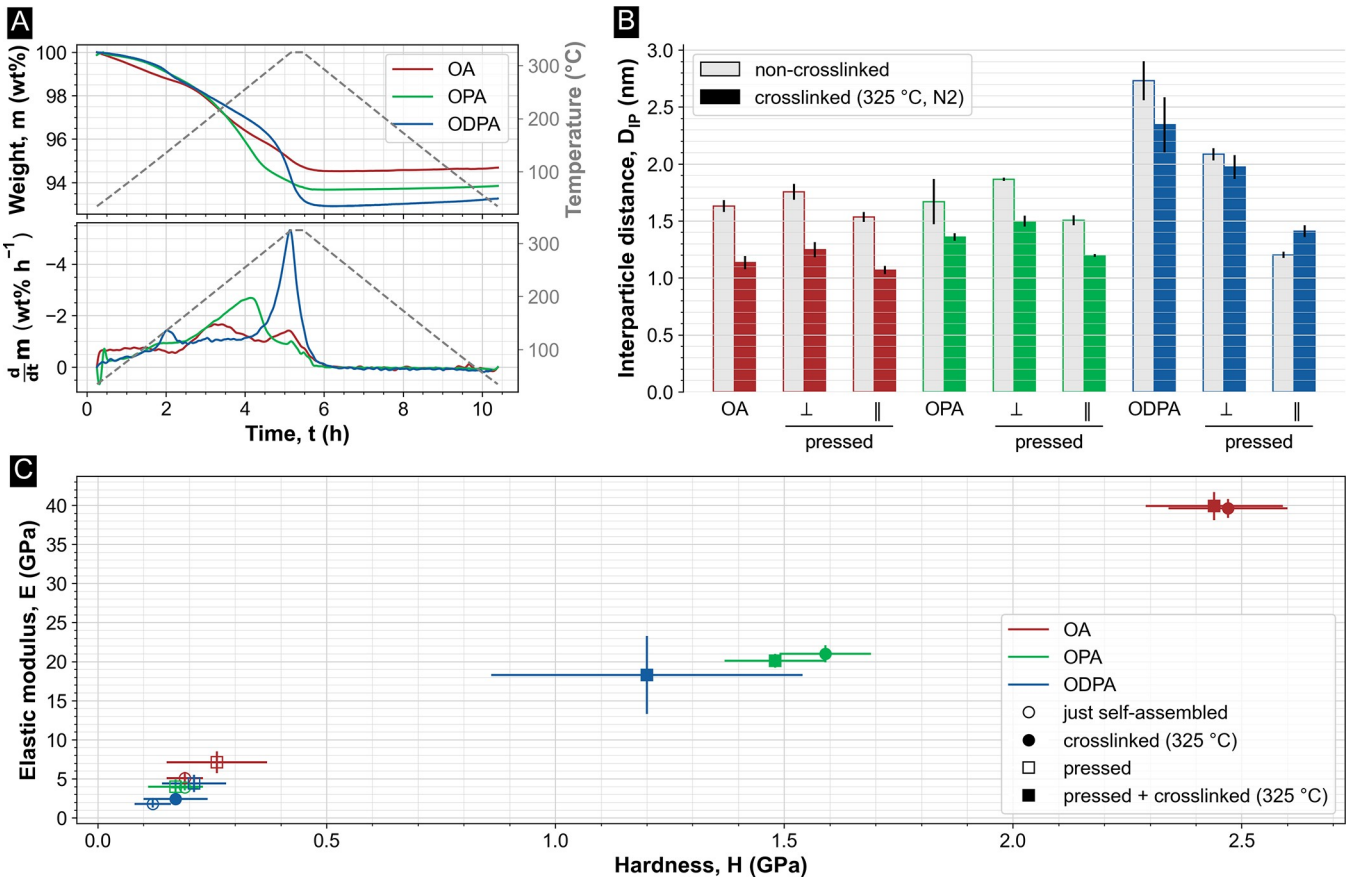

Figure 2. (A) Weight changes over time as obtained by TGA (top) and the corresponding derivative weight loss curves (DTG, bottom) during heat-treatment-induced cross-linking of the different NC@ligand systems under N_2. (B) Interparticle distances, D_{IP}s, obtained via SAXS for as-assembled (empty bars) and cross-linked under N_2 (filled bars) materials. For pressed SCs, the D_{IP} is calculated depending on the relative orientation to the applied load (either perpendicular, ⊥, or parallel, ||). (C) Elastic modulus and hardness values for the different materials with or without cross-linking and with or without pressing step.

peaks, which correlates with the average superlattice domain size, indicates larger crystalline domains for Fe_3O_4@OA > Fe_3O_4@ODPA > Fe_3O_4@OPA. Since the size distribution of the starting NC suspensions does not differ significantly between the three studied systems (Figure 1G), we relate the lower stability of the Fe_3O_4@OPA suspension to a faster and hence less controlled self-assembly, resulting in smaller SC domains. Furthermore, the distance between the superlattice planes in those SC materials obtained using ODPA functionalization is larger than for Fe_3O_4@OA and Fe_3O_4@OPA samples, as indicated by the shift to lower q-values of the (111) peak. Ultimately, this results in larger interparticle distances for Fe_3O_4@ODPA samples, as expected based on the stability model (compare the values shown in Figure 1H,I). Samples with ODPA functionalization present a 60% increase in D_{IP} compared to samples prepared with OPA ligand (i.e., 2.7 and 1.7 nm, respectively) from which ODPA solely differs on the saturation of one C=C bond. The stability model successfully predicted the D_{IP}s for Fe_3O_4@OA and Fe_3O_4@OPA (of 1.6 and 1.7 nm, respectively). However, the experimentally determined D_{IP} for Fe_3O_4@ODPA samples is larger than the predicted one (i.e., 2.7 and 2.0 nm, respectively). We attribute this difference to the saturation of the ODPA aliphatic chain, which directly affects its conformational entropy, not accounted by the stability model. All SC materials show, nevertheless, interparticle distances below the calculated length of the corresponding extended ligand molecule (Figure 1A). Therefore, the self-assembly results in superlattices in which the ligands interfacing the NCs are interdigitated and/or bent.

Surface Ligands As Reactive Platforms. The organic functionalization of inorganic cores allows for a further adjustment of the SCs' properties. It has recently been shown that when NC-interfacing organic ligands are cross-linked via a mild annealing step under inert atmosphere, the robustness of the SC materials is substantially increased.[4,5,7,13−16] Even if the effects of the cross-linking in the overall mechanical response are clear, neither the cross-linking mechanism nor the exact role played by the NC-interfacing phase (before and after cross-linking) have yet been resolved.[4,23,58−61] Therefore, aiming to understand the implications of the ligands when used as reactive platforms, a heat-treatment step to cross-link the organic ligands on the Fe_3O_4 NCs' surface was applied. Following previous studies, this cross-linking step proceeds under N_2, at 325 °C for 0.3 h.[13−15] After this annealing, all materials experience a weight loss of ca. 5.5−7.1 wt % (Figure 2A), while the periodic nanostructures are preserved (Figure S6), although a decrease in the superlattice constants, and therefore of the interparticle distances, is observed (Figure 2B). Moreover, energy-dispersive X-ray spectroscopy (EDX) evaluation of a sample with a phosphonate anchoring group (Fe_3O_4@OPA) confirms the presence of C and P around the NCs cores after heat treatment (SI Section 3.1), thus ensuring the presence of

https://doi.org/10.1021/acsnano.2c01332
ACS Nano 2022, 16, 11692−11707

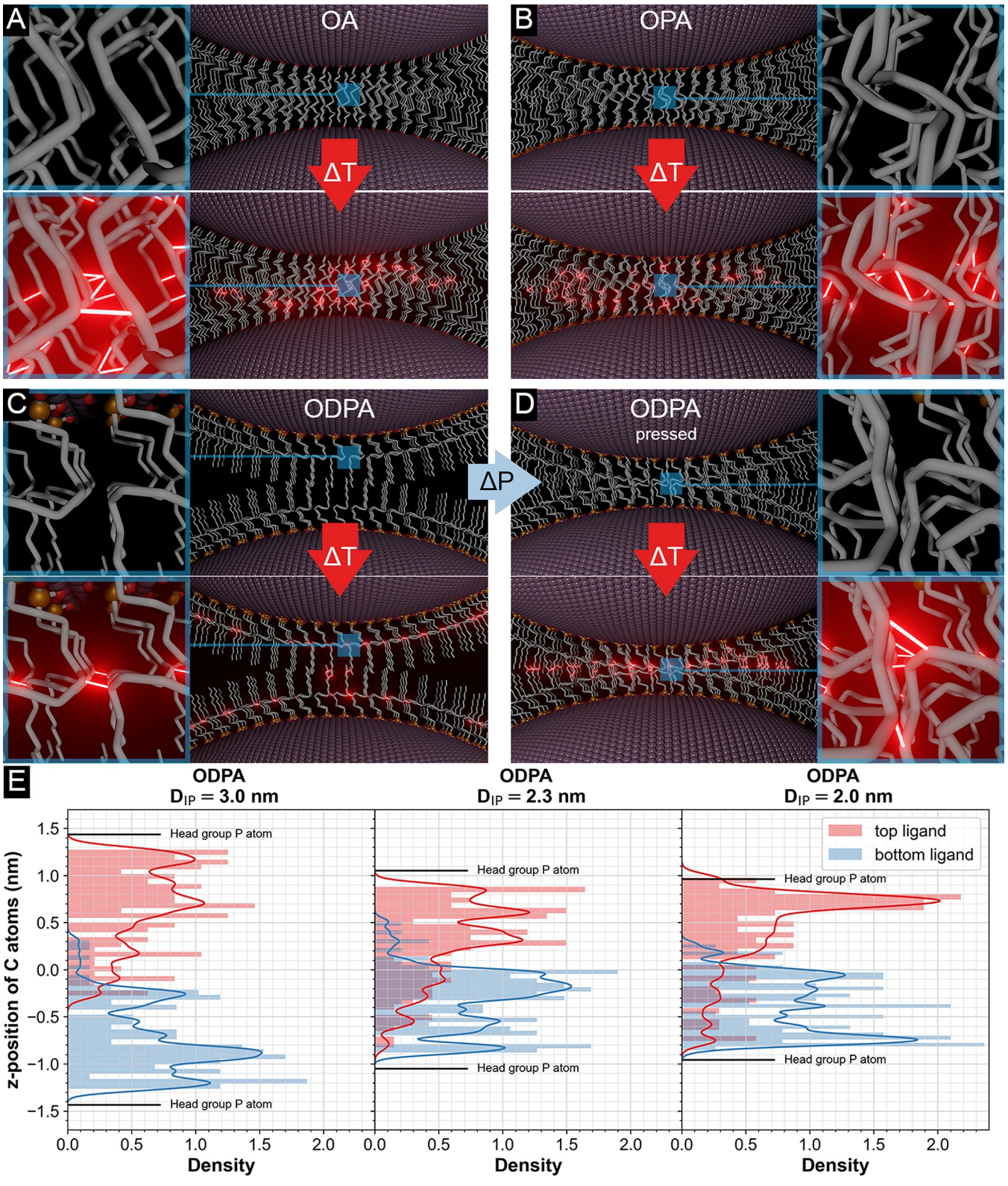

Figure 3. 3D model of two neighboring functionalized NCs, with zoomed-in insets showing interfacing ligands before and after cross-linking (indicated by the ΔT arrows). For simplicity, only the aliphatic backbone is displayed. Possible new bonds created after cross-linking between C atoms closer than ~1.6 Å (ca. length of a C−C bond) are highlighted in red. For further information see SI Section 3.3. (A) Fe_3O_4@OA and (B) Fe_3O_4@OPA systems. (C) Fe_3O_4@ODPA system without pressing and (D) with a pressing step before the heat treatment, as indicated by the ΔP arrow. (E) Distribution of the C atoms positions for two interfacing ODPA ligands fixed at different interparticle distances obtained via AIMD simulation. Larger interparticle distances clearly show a decreased interdigitation as indicated by the overlap region of the *z*-positions of C atoms.

https://doi.org/10.1021/acsnano.2c01332
ACS Nano 2022, 16, 11692−11707

organic matter at the NCs interfaces even after the thermal treatment. Note that when applying heat-treatment temperatures above 350 °C to similar materials (Fe_3O_4@OA), they suffered from sintering processes, resulting in a loss (or transformation) of the nanoarchitecture and thus a change in the NC-derived functional properties.[7,13,16,62,63] Sintering is promoted by the decomposition of the organic ligands interfacing the NCs cores, since the absence of interfacing ligands facilitates atom mobility between NC surfaces and thus a diffusion-driven damage to the overall NC-superlattice. Moreover, changes in the chemical composition of the NCs can also be promoted by high-temperature treatments,[62] directly impacting the resulting functional properties. Understanding the ligands' thermal behavior is, thus, imperative to avoid a detriment of functionality while gaining robustness.

Just self-assembled and cross-linked SC materials were mechanically evaluated via nanoindentation. Given the almost linear relation between elastic modulus and hardness usually observed for these materials,[13,14,64] in the following we will only discuss elastic modulus changes. As shown in Figure 2C, the elastic modulus (E) of Fe_3O_4@OA nanocomposites increases from 5.1 to 39.6 GPa after heat treatment. The elastic modulus of the interfacing ligands, E_L, is calculated by applying the rule of mixtures for parallel oriented layers perpendicular to the indenting direction (see SI Section 3.2). Before and after annealing, E_L for OA changes from 2.2 to 18.7 GPa, respectively. These values correspond well to finite-element method calculations and experimentally derived values for similar systems.[13,23]

When OPA is used as interfacing ligand, a rather moderate increase in elastic modulus (from 3.9 to 21.0 GPa, without and with cross-linking) is achieved, which results in elastic moduli of the ligands of 1.9−9.8 GPa, respectively. This increase is significantly smaller than the one observed for Fe_3O_4@OA nanocomposites. This is indeed a surprising result, since phosphate-derived ligands are known to form strong interactions to metal oxide surfaces, even stronger than carboxylates,[40−42] and therefore, a better material's cohesion with the consequent boost in the mechanical response was expected.

For ODPA, no significant increase of the elastic modulus is observed after annealing (blue circles in Figure 2C, 0.9 and 1.2 GPa, before and after heat treatment, respectively). The absence of strengthening after annealing fits very well with the expectations based on previous studies, where the working hypothesis relied on the presence of an unsaturated C═C double bond to promote cross-linking between adjacent ligand chains.[7,13] Nevertheless, after heat treatment, Fe_3O_4@ODPA materials present a similar weight loss to that of the other systems (Figure 2A) plus a similar decrease in interparticle distance (Figure 2B), indicating that akin chemical reactions are occurring in the three studied systems. Noteworthy, the interparticle distance for as-assembled structures of Fe_3O_4@ODPA is ∼1 nm larger than for the other systems.

It is thus plausible that the absence of strengthening when ODPA is used as a surface ligand is also related to a poor interdigitation of adjacent ligands, ultimately leading to a cross-linking reaction within each individual NC ligand-shell instead of between ligands from neighboring NCs (Figure 3C in comparison to A and B). In fact, the smaller elastic modulus obtained for ODPA ligands indicates a softer response of ODPA interfacing ligands right after self-assembly, as would follow from a larger conformational freedom of their alkyl chains due to a decreased ligand confinement within the obtained superlattices (in comparison with the other studied systems). To investigate the latter possibility, a pressing step in a rigid die at 150 °C was implemented after self-assembly, aiming toward a superlattice compression along the direction of the applied uniaxial load and thus an increased ligand interdigitation, as depicted in Figure 3D.[14] Pressed Fe_3O_4@ODPA nanocomposites show now a significant reduction in interparticle distances, $D_{IP\parallel}$ and $D_{IP\perp}$ (parallel and perpendicular to the load) from initially 2.7 nm down to 1.2 and 2.1 nm, respectively. The corresponding calculated superlattice strains indicate that the compaction of the FCC superlattice for Fe_3O_4@ODPA samples is more significant in the direction of the applied load (8.8% in the parallel direction, and 3.7% in the perpendicular one, see SI Section 3.2). When this pressed material is now heat-treated, the elastic modulus increases from 4.4 to 18.3 GPa (squares in Figure 2C), resulting in a much stiffer response of the ligands (E_{ODPA} = 8.6−9.6 GPa, Table S3) and ultimately reaching similar values to the ones obtained with OPA ligand.

It is important to note that for the other two systems, Fe_3O_4@OA and Fe_3O_4@OPA, no significant effect of the pressing in neither D_{IP} (i.e., superlattice strains around or below 1%, which falls within the error of the measurement) nor in the mechanical properties is observed. For these two systems, the measured interparticle distances right after self-assembly are below the length of a single ligand molecule. It is therefore plausible that the space between neighboring NCs is completely filled with highly confined OA or OPA ligands, not allowing for any further superlattice compaction.

In order to better understand the possible implications of the different interparticle distances in regards to the ligand conformation, interdigitation, and further cross-linking, we developed a simple, qualitative 3D model with a ligand geometry predefined based on the above-mentioned observations (further information in SI Section 3.3). As shown in Figure 3A,B, at a measured distance of 1.6 and 1.7 nm (Fe_3O_4@OA and Fe_3O_4@OPA, respectively), the ligands of adjacent NCs are interdigitated, and the C atoms of ligands attached to opposite NCs are at small distances. These close distances (when around the length of a C−C bond) allow their cross-linking upon heating, as depicted by the red lines. For larger D_{IP}s (up to 2.7 nm, as in the case of Fe_3O_4@ODPA) and as shown in Figure 3C, the overlap between adjacent ligands significantly decreases. By the additional uniaxial pressing of the obtained materials, the D_{IP} for ODPA is decreased down to 1.2 nm. Ab initio molecular dynamics (AIMD) simulations (SI Section 3.4) of ODPA ligands fixed on flat surfaces confirm that smaller D_{IP}s lead to an increased interdigitation of oppositely attached ligands. Already after relaxation (for 5 ps at 400 K), ligands, which were initially arranged in a coiled conformation with no interdigitation, start to rearrange leading to interdigitated structures, as shown in Figure S10. The figure of merit for the interdigitation is here represented by the overlap of the distributions of C atom positions (as projections in the z dimension) corresponding to ligands fixed at the top or at the bottom layers. It can be clearly seen that when decreasing the interparticle distance, the interdigitation of ligands (overlap region for C atom positions) gradually increases (Figure 3E). The observed asymmetry in the overlap region, in particular at interparticle distances of 2.3 and 2.0 nm, can be explained by differences in the initially generated atom velocity vector orientations. Note that for the AIMD

https://doi.org/10.1021/acsnano.2c01332
ACS Nano 2022, 16, 11692−11707

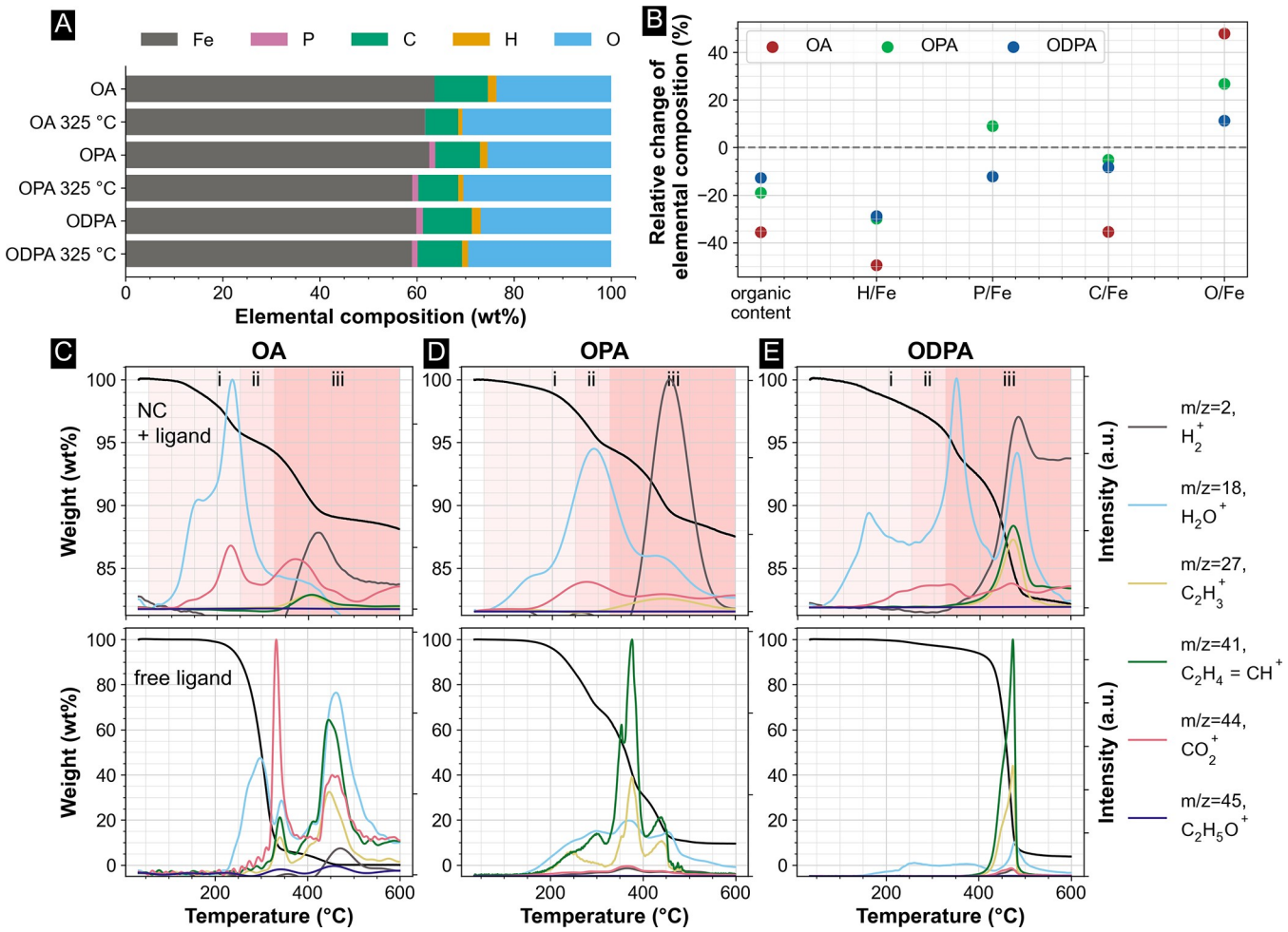

Figure 4. (A) Chemical composition as determined by EA of the NC@ligand from the starting suspensions and the SC materials after thermal cross-linking (without compression) under inert treatment (325 °C, N_2) and (B) the corresponding relative changes in elemental composition. Relative changes are expressed as the ratio between heat-treated samples and starting suspensions. Positive values imply an increase in elemental composition after cross-linking, and negative values a loss. Detailed information can be found in SI Section 3.5. (C–E) Results from the TGA-MS under argon showing the TGA curves (black) and the intensity of the major fragments detected in the gas phase by mass spectrometry for each of the NC@ligand systems used (top) and of the corresponding free ligands (bottom). From left to right, Fe_3O_4@OA,Fe_3O_4@OPA, Fe_3O_4@ODPA. The highlighted areas in the TGA-MS correspond to the three regimes proposed to describe the thermal processes. Further signals can be found in Figure S13.

simulation, flat layers were used to fix the top and the bottom ligands; however, in the real scenario and as can be seen in Figure 3C, only a small interparticle region is actually at the measured interparticle distance (i.e., 2.7 nm), while the distance between ligands of adjacent NCs increases when moving in the *x* and *y* dimensions due to the spherical nature of the particles.

The unexpected trend in mechanical properties (i.e., stiffer response for Fe_3O_4@OA than Fe_3O_4@OPA and the observed strengthening occurring for Fe_3O_4@ODPA compressed samples) indicates that the cross-linking reaction does not require the presence of a C=C double bond and that the overall cohesion of the material does not only profit from anchoring groups with a stronger binding affinity to the NC surface. Moreover, these findings denote that the cross-linking mechanism acting on these systems still remains to be understood.

Elemental analysis was used to gain insights into the composition of the remaining phases after the cross-linking step and to understand its implications in the overall materials' mechanical response. Figure 4A,B presents the chemical composition of the NC@ligand of the starting suspensions and the results obtained for the heat-treated materials (without compression). As expected, the organic content after heat treatment is reduced (between 13% and 30% depending on the ligand), with the major losses in the form of C and H. In general, Fe_3O_4@ODPA changes before and after the cross-linking step are minor, while for Fe_3O_4@OPA and Fe_3O_4@OA, these are more significant. For those samples with phosphate-derived ligands, no significant change in the P content is observed (the changes listed in P/Fe at%-ratio are due to the small fluctuations in the Fe-content relative to the low absolute P content of ca. 0.7%, SI Section 3.5). It can therefore be concluded that no change in the ligands grafting density (as number of anchoring groups per NC surface unit) occurred during heat treatment. This correlates well with previous studies from our group in which X-ray photoelectron spectroscopy (XPS) and ultrahigh-vacuum infrared spectroscopy confirmed the stability of the anchoring groups to the NC surface in similar systems (magnetite NCs with carboxylates or phosphate-derived ligands).[13,14] Interestingly, the O content is increased after cross-linking (between 10% and 24%, depend-

https://doi.org/10.1021/acsnano.2c01332
ACS Nano 2022, 16, 11692–11707

ing on the ligand), pointing toward oxidative processes occurring during cross-linking.

In order to in situ follow the thermal evolution of the as-prepared (noncompressed) SC materials and the free ligands, thermogravimetric analyses coupled with mass spectrometry (TGA-MS) were carried out under inert atmosphere (Ar), see Figure 4C–E. Although the thermal evolution of these SC materials is an intricate process, it can be divided into three main temperature regimes—the exact position of each regime being affected by the ligand used—as follows: (i) 50–250 °C, (ii) 250–325 °C, and (iii) >325 °C. In the first regime (i), mainly the presence of H_2O^+ and OH^+ is detected, with the reactivity order Fe_3O_4@OA > Fe_3O_4@ODPA > Fe_3O_4@OPA. CO_2^+ and CO^+ appear at the upper end of this temperature range for the phosphate-derived ligands, although with minor intensity, while for Fe_3O_4@OA, the first CO_2^+ peak is already observed at ca. 230 °C.

In the second regime (ii), the same species as in (i) evolve, but now CO_2^+ and CO^+ become more prominent also for the phosphate-derived ligands. Other minor species do not appear in either of these two steps. At temperatures >325 °C (regime (iii)), a cascade of reactions occurs, resulting in a myriad of signals associated with fragmentation products (aliphatic, alkenyl, and alkoxy fragments). It is also important to note that the presence in the gas phase of P-derivative species (e.g., m/z = 47 or 65, associated with PO^+ or $H_2PO_2^+$, respectively)[65,66] is not detected for any of the studied samples, again confirming the stability of the anchoring group to the NC surface. These results evidence that, while the three anchored ligands behave in a similar way in terms of the evolved chemical species under thermal inert treatment, the temperatures for the reactions' maximum conversion highly depend on the type of ligand. TGA and DTG curves presented in (Figure S2C) indicate two significant weight changes. When comparing the relative DTG peak positions (indicative of the position of the weight curves inflection points) for each NC@ligand system, the first inflection points are found at ca. 220 °C for Fe_3O_4@OA, 280 °C for Fe_3O_4@OPA, and 340 °C for Fe_3O_4@ODPA.

Interestingly, and in contraposition to SC systems, the thermal behavior of the free ligands (i.e., not bound onto a NC surface) under Ar atmosphere differs dramatically, Figure 4C–E, bottom. The start of the reaction is now shifted to higher temperatures (reactivity order by ligand OPA ≥ OA ≫ ODPA), and almost simultaneous multiple signals related to different fragmentation and molecular rearrangement processes are detected, pointing toward a complete decomposition of the free ligands. The main MS peaks are consistent with alkene (e.g., m/z = 41, 42) and carboxylic/epoxide (e.g., m/z = 43, 55) cleavage reactions. We attribute the lower temperatures needed to react NC-anchored ligands, compared to the corresponding free ligands, to a catalytic activity of the magnetite surface. Moreover, the appearance of H_2O^+/OH^+ together with CO_2^+ /CO^+ gives a strong hint that the ligand molecules suffer oxidative processes despite the inert atmosphere. The source of oxygen for such oxidative processes within the SC materials is not evident nor trivial to identify. Some authors have claimed that the appearance of H_2O and CO_2 at these low temperatures could be explained by the presence of weakly physically bound ligands and decarboxylation-like processes.[67,68] Given that the anchoring groups remain in the system, as inferred from EDX and EA and as already proven by previous studies,[7,13,14] and the comparable appearance of CO_2 for the three systems, it is highly improbable that these signals are only the result of anchored head groups suffering from decarboxylation-like processes at the used cross-linking temperature. We therefore hypothesize that oxygen migration and restructuring of the near magnetite surface explains the observed increase in oxygen content (Figure 4B). If oxygen from the catalyst surface (i.e., the NC core) is transferred into the organic phase during inert heat treatment, the magnetite cores would suffer from reductive processes. Subsequent exposition of the materials to air would cause a reoxidation of the catalyst to its initial composition.

XPS was used to obtain more insight into the chemical composition of the magnetite surfaces during the annealing process. As can be seen in Figure 5A, a Fe_3O_4@OA NCs (the most reactive system) thin film deposited on a silicon substrate shows the presence of the magnetite phase, inferred by the appearance of two sharp peaks at 710.7 and 724.0 eV, corresponding to Fe $2p_{3/2}$ and Fe $2p_{1/2}$, respectively.[13,14] When the deposited film is in situ heat-treated up to 150 °C under high vacuum, new signals appear as shoulders toward lower binding energies, indicating a reduction of the iron species. These new signals gradually rise with increasing temperatures, becoming clearly visible above 300 °C. Interestingly, the appearance of Fe-reduced species upon annealing was not observed in previous ex situ XPS studies on similar systems.[10,13,14] This is most probably related to the reoxidation of the catalyst surface after exposition to air. The ultimate identification of the Fe-species formed is, though, challenging. In situ X-ray diffraction analyses under N_2 atmosphere of Fe_3O_4@OA only revealed changes in the iron oxide lattice well above the temperatures used in this study (Figure S12). We attribute this to the bulk resolution of the technique, which does not allow to isolate surface-derived changes from the overall NC response.

Strong differences with increasing temperature also arise in the C 1s core level shown in Figure 5B. Initially, a sharp peak at 284.5 eV corresponding to C(sp^3) of the aliphatic chain is observed, accompanied by broad peaks related to C–O containing species at 285.4 eV attributed to the surface bound ligand headgroup. A signal at higher binding energies corresponding to further oxidized species (at 286.6 eV) rises upon increasing temperatures, ultimately confirming the hypothesis of oxygen migration from the magnetite lattice into the organic phase, in line with the observation in the Fe 2p core level and the reduction of iron in the oxide phase.

The catalytic activity of the NC core surface can furthermore explain the different reactivities of the NC@ligand systems. The higher reactivity for OA system compared to OPA one (from which it only differs in the anchoring group to the NC surface) can be associated with changes in the interaction between the anchoring group and the magnetite catalyst surface. This is plausible, since adsorbed/bound species at the NC surface can significantly alter the near surface properties.[18,31,32,69] On the other hand, the different reactivity of OPA compared to ODPA (both, free and within the superlattice) is most likely related to the presence of a more reactive C=C bond, in comparison to the simple C–C bonds present in ODPA.[70]

Cross-Linking Mechanism of NC-Interfacing Ligands. The results presented thus far indicate that the cross-linking mechanism is based on oxidative processes catalyzed by the magnetite surface. We relate this mechanism to oxidative reactions similar to the ones occurring in lipids, for example,

https://doi.org/10.1021/acsnano.2c01332
ACS Nano 2022, 16, 11692–11707

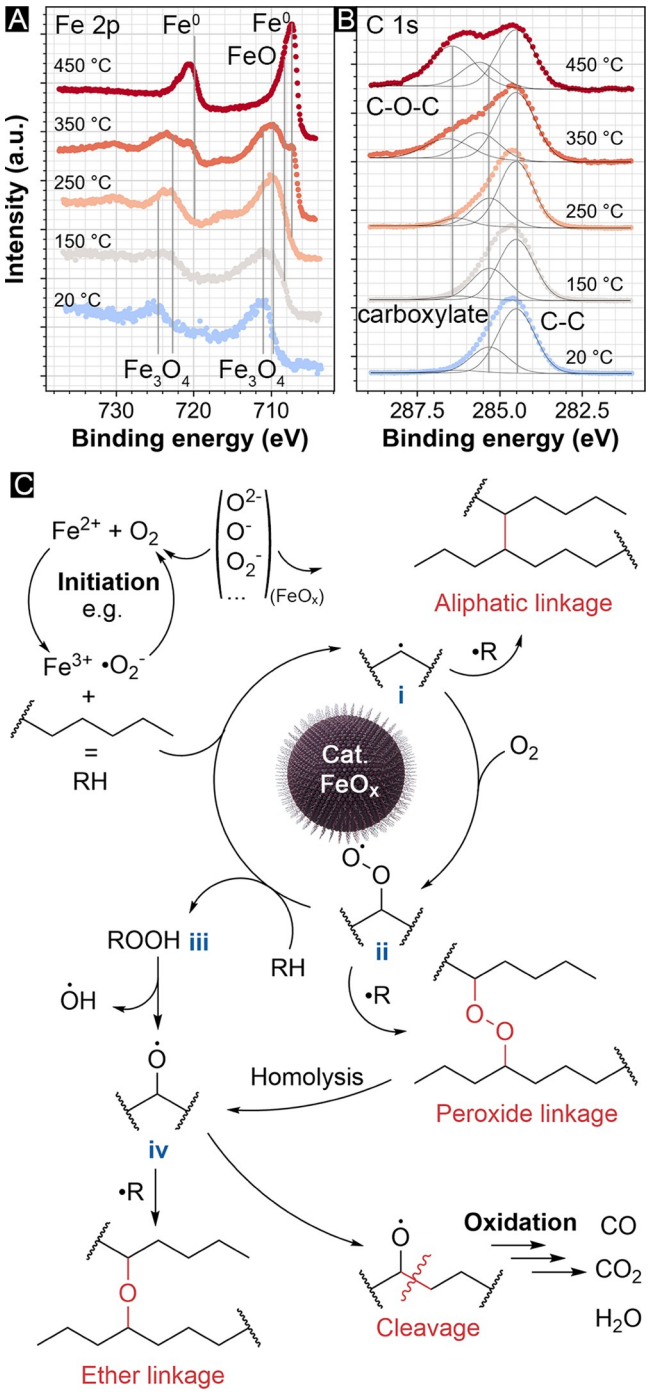

Figure 5. High-resolution XPS (A) Fe 2p and (B) C 1s core level with the corresponding deconvolved identified peaks of a Fe_3O_4@OA thin film in situ heat-treated from 25 to 450 °C under vacuum. (C) Proposed reaction steps during cross-linking of Fe_3O_4-anchored ligands leading to a broad set of active intermediate compounds (i–iv) and different cross-linking linkages (in red) of adjacent ligands.

fatty acids and phospholipids, resulting in oxidative polymerizations, which are known to be promoted by thermal processing, metal catalysis, or exposure to light.[68,71−81] Therefore, the cross-linking reaction emerges as being susceptible to modifications based on the ligands' chemical structure, heat-treatment temperature, and heat-treatment atmosphere.

Oxidative polymerizations are radical processes with three main events: initiation, propagation, and termination. The initiation step is quite complex and not yet fully understood; however, it is believed to involve the abstraction of a labile hydrogen atom from the fatty acid aliphatic chain and thus formation of an aliphatic radical R• (Figure 5C(i)). This step takes place via metal catalysis where oxygen is the active species involved.[79] In the case of Fe species, an ion-mediated electron-transfer mechanism can create reactive oxo-radicals $O_2^{-\bullet}$,[80−83] supporting the herein inferred involvement of the NC core. Further reactive species of oxygen may be surface-bound O^{2-}, O^-, O_2^-, originating from the same Fe_3O_4 lattice when the cross-linking is done under inert atmosphere.[84,85] The aliphatic position from which the hydrogen is removed depends on the electronic environment within the aliphatic chain.[71,77] In unsaturated acids (as for OA and OPA), the initial radical (R•) is generated preferentially adjacent to a double bond, since the formed free radical is stabilized with a resonant structure. Decreasing the number of double bonds, as in the case of ODPA, makes of course the oxidizability less significant, since the monoallylic methylene hydrogens are more resistant to abstraction,[86] which explains the observed lower reactivity found for ODPA compared to OPA.

After the initiation step, the obtained aliphatic radicals further react with oxygen to form peroxyl radicals, ROO• (Figure 5C(ii)). In the presence of good hydrogen donors, for example, neighboring ligand chains, the peroxyl radicals can form hydroperoxides, ROOH (Figure 5C(iii)). These hydroperoxides are unstable and thus further break down to more peroxyl or alkoxyl radicals, RO• (Figure 5C(iv)), promoting a wide range of volatile, secondary oxidation products and aliphatic radicals. The decomposition of hydroperoxides is more likely to occur through cleavage of the O−O bond of the hydroperoxide to form alkoxyl and hydroxyl (OH•) radicals, as O−O bond cleavage (ΔE = 44 kcal/mol) is thermodynamically more favored than that of O − H (ΔE = 90 kcal/mol).[77,79] This relates well with the strong appearance of OH^+ and H_2O^+ fragments already observed at low temperatures in the TGA-MS analysis (Figure 4). Moreover, while the volatile oxidation products and aliphatic radicals were well observed in the TGA-MS of the free ligands, for the NC@ligand systems, these fragments were most likely further oxidized by the NC catalyst surface and appearing as CO^+ and CO_2^+ signals.

The generated alkoxyl (RO•), peroxyl (ROO•), hydroxyl (OH•), and new aliphatic radicals (R•) meanwhile can further participate in the chain reactions of free radicals. In the oxidation termination step, radicals neutralize each other through radical−radical recombination or radical−radical disproportionation to form stable nonradical products. These nonradical products are then the result of the overall cross-linking reaction between neighboring ligand aliphatic chains, which has proceeded via either aliphatic, ether, or peroxide linkage of two neighboring chains. The latter most likely homolytically dissociates into radical (iv) species, due to the lower dissociation enthalpy of dialkyl peroxides compared to hydroperoxide (iii) species.[87] Other possible final products result from aldol condensation reactions (with the consequent release of water, as observed via TGA-MS) or the formation of hydroperoxy cyclic peroxides and further decomposition by chain scission of the same.[73,74]

The newly formed oxidized bonds are confirmed in the C 1s region of the XP spectra at 286.4 eV, corresponding to C−O−C species (Figure 5B).[88] The O 1s region (Figure S11) also

https://doi.org/10.1021/acsnano.2c01332
ACS Nano 2022, 16, 11692−11707

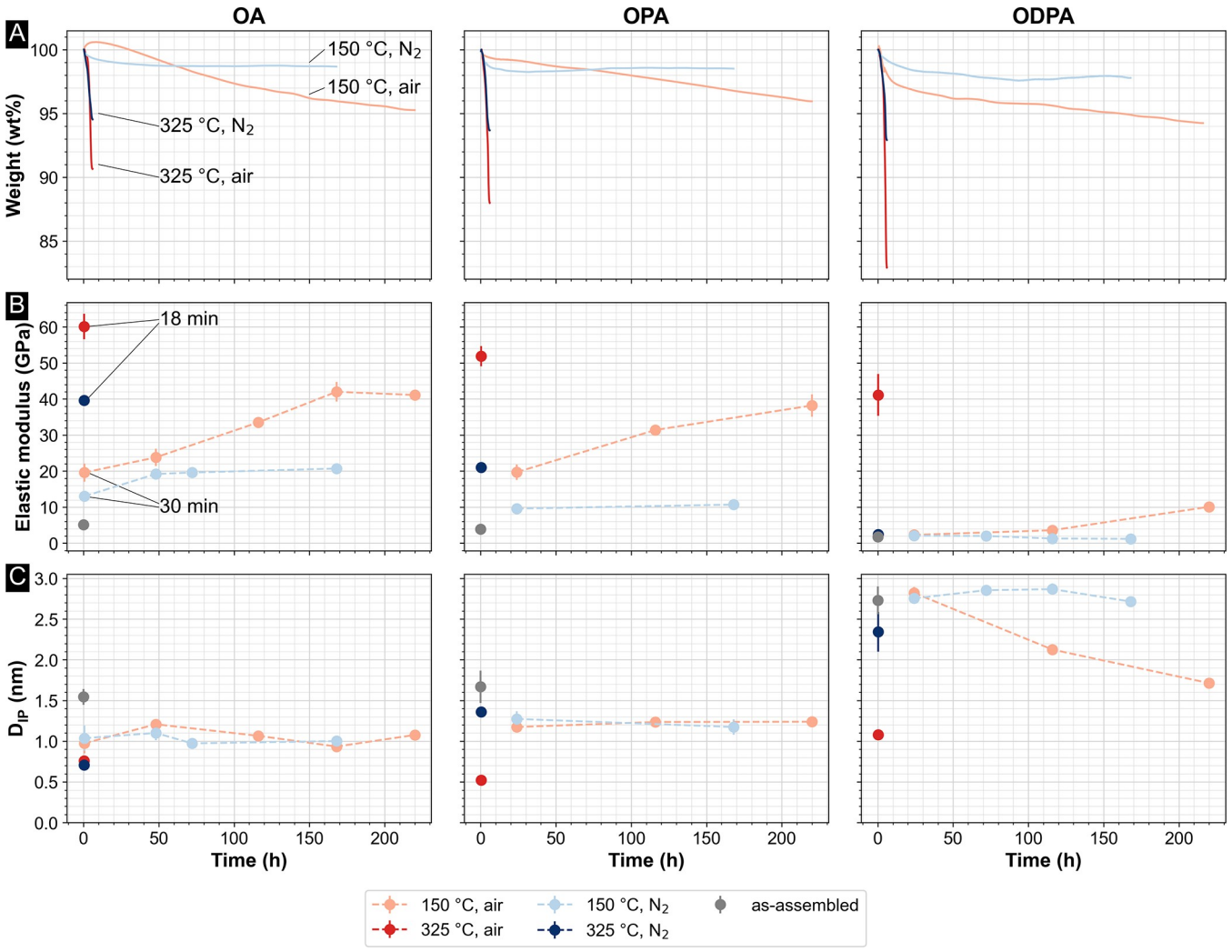

Figure 6. Summary of the effects of the different heat treatments versus time for all studied ligands under different temperatures and under either nitrogen (N_2) or ambient conditions (synthetic air). (A) In situ weight changes during heat treatment, as obtained via TGA. (B) Change in elastic modulus and (C) interparticle distance, D_{IP}, over time. For the heat treatments at 325 °C, only one heat-treatment time was investigated because longer heat treatments did not change the mechanical properties under N_2, as implied by the saturation in weight loss shown in Figure 2A.

shows a gradual increase of a C−O peak around 532 eV. However, a strong Si−O signal arising from to the silica substrate hinders the proper deconvolution of the peaks in this region.

It can be ultimately concluded that the oxidative process is most likely a cascade reaction leading to different types of new cross-links (i.e., C−C and C−O−C) between neighboring ligands. Although these new cross-links are preferentially created adjacent to the C═C double bond for unsaturated ligands, the results obtained with ODPA ligands indicate that the reaction can also proceed at the saturated part of the ligand backbone, and therefore, multiple cross-links per ligand chain are plausible, leading to a polymeric network throughout the SC material. It becomes clear that the cross-linking reaction, and thus the materials' mechanical behavior, can be significantly altered by temperature and the presence of oxygen.

Tuning the SC's Nanostructure and Mechanical Properties. To better elucidate the influence of oxygen in the cross-linking mechanism, further heat treatments under an oxygen-rich atmosphere were performed. In situ TGA-MS under 20% O_2−Ar mixture of self-assembled samples indicate similar temperature regimes, as observed when using an inert atmosphere (compare Figure 2C and Figure S14). Between 50 and 250 °C (regime (i)), the main signals detected correspond to H_2O^+, OH^+, while CO_2^+ (and CO^+) and other minor species associated with fragmentation products (e.g., $C_2H_5^+$, $CH_2CHCH_2^+$, or $CO_2H^+/C_2H_5O^+$) only start to appear. In the next temperature range (250−325 °C, regime (ii)), the CO_2^+ species start to appear with a stronger intensity, while no significant aliphatic fragments are observed. Above 325 °C (regime (iii)), the CO_2^+ species appear with a stronger intensity, while aliphatic fragments are less significant than under inert atmosphere, most likely due to a complete oxidation promoted by the additional oxygen supply.

To relate the presence of oxygen during heat treatment to the material's mechanical response, each material system was heat-treated over different periods of time under ambient conditions and tested via nanoindentation. For a proper comparison between heat-treating atmospheres, the same time intervals and temperatures were also applied under N_2. Since TGA-MS indicated a first reaction step at ca. 150 °C with no

https://doi.org/10.1021/acsnano.2c01332
ACS Nano 2022, 16, 11692−11707

significant fragmentation products observed (Figure 4), this temperature was chosen as a possible cross-linking temperature. Moreover, the slower weight loss arising from this heat-treatment temperature allows a better time-resolved investigation of the ongoing processes. To avoid uncontrolled cross-dependencies between parameters, none of the SC materials used in this part of the study was pressed.

At 150 °C under N_2, and as seen in Figure 6A, the weight starts to rapidly decrease until reaching a plateau after ca. 70 h, exact time depending on the material system, as Fe_3O_4@OPA < Fe_3O_4@OA < Fe_3O_4@ODPA. While for Fe_3O_4@ODPA, no significant increase in E is observed under these conditions, for Fe_3O_4@OPA and Fe_3O_4@OA the elastic modulus (Figure 6B) undergoes a rapid increase until it reaches a maximum after which it remains constant, in agreement with the recorded weight loss. Both plateaus, in weight and in elastic modulus, coincide in time. The maximum elastic modulus achieved is found at ca. 20 and 10 GPa for Fe_3O_4@OA and Fe_3O_4@OPA, respectively. As seen in Figure 6C, a slight decrease in interparticle distance accompanies the observed changes. Within the first 30 min and for Fe_3O_4@OA and Fe_3O_4@OPA SC materials, the D_{IP} decrease is ca. 0.4−0.5 nm and concurs with the highest weight losses observed. Afterward, the D_{IP}s do not change significantly over the whole time range. For Fe_3O_4@ODPA, the weight loss at 150 °C under N_2 does not impact the D_{IP}s, which remain constant (changes inside the error of the measure) for the whole heat-treatment time.

Heat-treating at 150 °C under ambient conditions provokes different effects on the systems. For all the studied materials, the mechanical properties are significantly increased versus the corresponding inert heat treatment. Moreover, less significant initial weight losses (up to ca. 70−100 min reaction times, depending on the system) are observed (see red curves in Figure 6A). For Fe_3O_4@OA SC materials, an initial increase in weight within the first 8 h is also observed. This weight increase is a strong indication of oxygen uptake from the environment, in agreement with the EA results in Figure 4. After this initial increase, the weight decreases almost linearly. For all of the materials within the investigated 220 h, no weight plateau is reached. Moreover, the almost linear weight loss correlates with a gradual increase in elastic modulus, while the SC structures are maintained (see Figure S16). Concretely, Fe_3O_4@OA and Fe_3O_4@OPA materials even reach values of ∼40 GPa, which corresponds to the maximum value obtained for Fe_3O_4@OA at 325 °C under N_2. Contrary to what was observed for 325 °C under inert atmosphere, now the materials obtained with OA and OPA surface functionalized NCs boost their mechanical response without relevant D_{IP} changes (maximum decrease in D_{IP} within 0.5 nm, Figure 6C). For Fe_3O_4@ODPA SC materials, for which no change in the mechanical response could be observed under N_2 even at 325 °C, now a significant increase in E is achieved after ca. 100 h.

These observations complement the ongoing mechanism proposed above (Figure 5). The sharp initial increase in E and D_{IP} changes for Fe_3O_4@OA and Fe_3O_4@OPA within the first 30 min is attributed to the prompt reaction of the unsaturated C═C ligands, while the following slow linear trend is related to the reaction proceeding at the saturated carbon sites. This hypothesis is reinforced by the increase in E for Fe_3O_4@ODPA after 100 h having a slope similar to the one of Fe_3O_4@OPA. Eventually, under inert atmosphere, the reaction reaches a plateau, due to exhausted radical initiators. Under ambient conditions, with a constant supply of oxygen, this plateau is not reached within the considered time-frames. The late onset of increase in E for Fe_3O_4@ODPA under ambient conditions corresponds well to a ligand scission promoted by ligand rearrangement, accompanied by the observed decrease in D_{IP}. Once a certain overlap of adjacent ligands (or parts of them) is reached, as depicted in Figure 3, the cross-linking between neighboring NCs@ligands can finally proceed. For Fe_3O_4@OA and Fe_3O_4@OPA, this ligand scission most likely also occurs during the cross-linking reaction, but ligand rearrangement is hindered by the already cross-linked organic matrix.

These results indicate that the elastic modulus and hardness, and likely the material's strength since it typically scales with E for these material systems,[4,5,13] can be easily tuned by the surface ligands and the cross-linking reactions via temperature and atmosphere and not just by lowering the organic content (Figure S17) or the interparticle distances. Preserving the organic content and D_{IP}s are indeed important aspects to maintain the final materials' functionality and toughness, since the soft interphase is responsible of the load-carrying mechanisms.[4,15,17] Additionally, it becomes clear that interparticle distances can be easily and independently adjusted without significantly affecting the overall mechanical response, an important factor to tune the collective properties of functional nanomaterials while still maintaining a robust architecture.

Since oxygen had a positive effect on the strengthening of all three investigated material systems, we further conducted the heat treatment at 325 °C under ambient conditions. Even though this step promoted a substantial weight loss (Figure S15), the obtained materials preserved their nanoarchitecture without completely removing the organic interphase, as shown by the appearance of the FCC diffraction peaks (see Figure S16). Please note, similar materials[16] heat-treated at temperatures above 350 °C under N_2 showed a complete disappearance of the FCC SAXS diffraction peaks, as expected for sintered structures. Therefore, the heat treatments under oxygen at higher temperatures (325 °C) lead to significant decreases in D_{IP}s due to a stronger organic combustion, as indicated by the appearance of CO_2 in the TGA-MS, but still allowed to avoid sintering and the loss of the nanostructure-derived functionality.

Ultimately, the oxygen-containing environment promotes a significant boost of the mechanical properties, even at low temperatures, reaching values substantially higher than the ones obtained under N_2 atmosphere. Worth highlighting are the very high values of hardness and elastic modulus obtained (up to 40 GPa for the nanocomposites and up to 19 GPa for the organic phase), especially considering that these are hybrid materials in which one of the phases is an organic network derived from common fatty acids or organophosphates.

CONCLUSIONS

The understanding of the ongoing processes during NC self-assembly and supercystalline material reactivity is important to not only tailor the final materials' properties but also to identify new suitable material systems for engineering new, functional nanocomposite materials.

The effect of different surface ligands (oleic acic, oleyl phosphonic acid, and octadeyl phosphonic acid) in hybrid organic−inorganic NC systems has been studied in terms of supercrystal formation and further strengthening via thermal cross-linking. The use of ligands with the same number of C

https://doi.org/10.1021/acsnano.2c01332
ACS Nano 2022, 16, 11692−11707

atoms and similar grafting density leads to similar FCC superstructures of functionalized Fe_3O_4 spherical NCs. Neither the presence of an aliphatic unsaturation nor the anchoring group—phosphonic or carboxylic acid—influence the SC phase, and all the resulting interparticle distances are below the length of two (extended) ligand molecules, which implies that the interfacing ligands are interdigitated or bent.

However, small changes in the aliphatic backbone significantly alter the ligand conformation and stability in the starting colloidal suspensions, directly impacting the self-assembly and superlattice parameters. Interestingly, when a ligand with a saturated aliphatic chain is used, the superlattices present an almost two-fold gap between neighboring NCs, compared to ligands containing a C=C bond. This structural difference has a tremendous effect on the SC strengthening, since an insufficient interdigitation of adjacent ligands hinders their cross-linking. We demonstrated how this structural disadvantage can be easily solved by promoting a compaction of the superlattice, allowing a better ligand interdigitation of neighboring particles.

The specific NC@ligand reactivity as well as the annealing atmosphere and temperature during cross-linking have been identified as key parameters for material strengthening. We have shown how the strengthening proceeds via a cross-linking-based radical oxidative polymerization, catalyzed by the NC core material. The core catalytic activity, and thus extent of cross-linking, is significantly affected by the ligands anchoring group to the NC surface.

Moreover, the identification of oxidative processes governing the cross-linking reaction allowed us to adjust the cross-linking step. By using an atmosphere with oxygen, substantially lower temperatures (down to 150 °C, versus the proposed in previous studies, 325−350 °C)[13] are now required for the cross-linking step, avoiding possible temperature-induced nanostructural damage of the nanoarchitectures.

The gained insights are used to independently tune the mechanical properties and the interparticle distances of the obtained SC nanostructures simply by adjusting annealing temperature and atmosphere. This ultimately provides an opportunity to tune the mesostructural collective properties of functional nanomaterials while still maintaining a robust mechanical response, which are indispensable steps toward their application.

EXPERIMENTAL SECTION

Ligand Exchange and Starting Materials Characterization. Oleic acid-stabilized iron oxide NCs dispersed in toluene, Fe_3O_4@OA, (from CAN GmbH, Germany) were modified with OPA or ODPA via a ligand exchange reaction, following a procedure analogous to the one reported in a previous publication, here summarized for the reader's convenience.[89] The ligand exchange reactions for OPA and ODPA were performed in chloroform and THF, respectively. Hence, the iron oxide NCs were precipitated from the toluene suspension in a first step by adding acetone 1:1 (v/v) and collected via centrifugation (6000*g*, 6 min). The obtained pellets were redispersed, either in chloroform or THF, with a mass concentration of 40 g L^{-1}. For the ligand exchange with OPA, 7.9 g of the ligand was dissolved in 200 mL of chloroform, and 300 mL of the respective particle suspension was added under rapid stirring. After 48 h of stirring at room temperature, the NCs were precipitated by adding methanol 1:1.5 (v/v) and separated via centrifugation (8000*g*, 10 min). The obtained pellet was washed several times in pure methanol, supported by ultrasonic treatment, followed by magnetic separation of the NCs. Subsequently, the NCs were redispersed in fresh chloroform and characterized using Fourier-transform infrared spectroscopy (FTIR), TGA, and EA. The procedure of precipitation, washing, and characterization was repeated, until the characterization results indicated an organic content corresponding to the adsorption of a monolayer of OPA on the NCs' surface. After the final iteration, the NCs were redispersed in toluene. For the ligand exchange with ODPA, 2 g of the ligand was dispersed in 50 mL of THF, and 60 mL of the respective NC suspension was added under rapid stirring. After stirring for 24 h at room temperature, the NC suspension was purified according to the method described for OPA, but less methanol (1:1 (v/v)) was necessary for the precipitation. With only a monolayer of the ligand remaining in the sample, as determined via TGA and EA during the characterization step, the NCs were redispersed in fresh toluene.

Preparation of the Supercrystalline Nanocomposites. Starting suspensions of surface-functionalized NCs in toluene (Chemsolute, >99.7%) were self-assembled by slow evaporation of the solvent carrier within several days at room temperature in 10 mm inner diameter cylindrical vessels. The amount of materials used was the one needed to obtain 1 g of nanocomposite pellets. Just self-assembled samples were recovered after complete evaporation of the solvent (within 10 days) and dried under vacuum at room temperature. For pressed samples, the dried self-assembled samples were compressed under an uniaxial load of 50 MPa for 40 min at 150 °C. The temperature was previously optimized to ensure suitable rheology of the ligands during compression.[13]

Thermally induced cross-linking and in situ weight track were done at either 150 or 325 °C under 20 mL min^{-1} N_2 or synthetic air (20% O_2−N_2 mixture) flux with a heating and cooling ramp of 1 K min^{-1} using a TGA/DSC 1 STARe (Mettler Toledo).

Small Angle X-ray Scattering. The size and size dispersion and the obtained superlattices (before and after heat treatment) were evaluated via SAXS. The experiments were performed at the high-energy materials science (HEMS) beamline operated by Helmholtz-Zentrum Geesthacht at the PETRA III storage ring at the Deutsches Elektronen Synchrotron (DESY). The energy of the incident beam was 87.1 keV (wavelength: 0.01423 nm), and the beam size was (0.2 × 0.2) mm^2. A two-dimensional PerkinElmer detector with a pixel size of 200 μm was placed at a sample-to-detector distance of 3256 mm to detect the scattering signal. Background scattering of the experimental setup was subtracted from the data before further analysis. The fitting procedure was performed using self-developed Python code. The calculation of the particle sizes was performed via the particle form factor and the lattice parameters via the position of the (111) Bragg reflection. For further information, see SI Section 2.1. No radiation damage was observed for the chosen exposure times.

Scanning and Transmission Electron Microscopy. Scanning electron images were taken with a Zeiss Supra VP55 (Zeiss, Germany) at 1.5 kV, with 10 μm aperture size, in high vacuum mode, and using the Everhard−Thornley detector. Specimens were mounted on a SEM sample holder using silver glue (Acheson Silver DAG 1415 M). TEM bright-field images and corresponding selected area electron diffraction (SAED) patterns were recorded on a FEI Talos F200X (Hillsboro, OR, USA) operating at 200 kV and a beam current of 10 nA. Element distribution maps were recorded in STEM mode at 200 kV with a probe current of 1 nA. The resolution of the maps is 512 × 512 pixels with a pixel size of 384 pm. Only two of the four detectors of the SuperX G2 EDX detector system were used, due to shadowing from the TEM grid.

Thermogravimetric Analysis Coupled with Mass Spectrometry, Fourier Transform Infrared Spectroscopy, and Elemental Analysis. A Netzsch STA 449 F3 Jupiter, with SIC furnace, DTA-TG sample carrier, and QMS 403 Aëolos capillary coupling was used for the TGA-MS measurements. Samples were heated in DTA crucibles made of Al_2O_3 (0.3 mL) at a rate of 5 K min^{-1} from 30 to 600 °C in an Ar or synthetic air (20% O_2-Ar) with a flow rate of 40 mL min^{-1}. The weight losses and emission gases (selected mass number traces) that occurred during this time were simultaneously recorded and determined.

Attenuated total reflectance-Fourier transform infrared spectroscopy was performed using a Varian 660 FTIR spectrometer (Agilent,

https://doi.org/10.1021/acsnano.2c01332
ACS Nano 2022, 16, 11692−11707

Santa Clara, CA, United States) equipped with a Pike MIRacle single reflection ATR system (Pike Technologies, Madison, WI, United States). Suspensions of the samples were dried on the crystal, and resulting films were measured with a resolution of 4 cm^{-1} by averaging 64 scans.

Elemental analysis for carbon and hydrogen (C, H) was performed on dried powder samples (starting suspension) or milled powder samples of the HT materials using an Eurovector EuroEA3000 elemental analyzer. Prior to the analysis for iron and phosphorus (Fe, P), the respective powder samples were chemically digested by addition of a mixture of nitric and perchloric acid. The ion contents were determined using inductively coupled plasma-atomic emission spectroscopy on a SPECTRO Analytical Instruments SPECTRO ARCOS system.

X-ray Photoelectron Spectroscopy. The measurements were carried out in an ultrahigh-vacuum setup equipped with a high-resolution Specs PHOIBOS 150 2D-DLD elevated pressure energy analyzer on freshly deposited Fe_3O_4@OA-NCs on a silicon substrate.[90] Heat treatment of the substrate was performed in situ (from room temperature to 450 °C, at 10 K min^{-1}). A monochromatic Al Kα X-ray source (1486 eV) was used. The base pressure was around 2×10^{-10} mbar. Spectra were recorded in the fixed transmission mode. A pass energy of 20 eV was chosen, resulting in an overall energy resolution exceeding 0.4 eV.

In Situ X-ray Diffraction. The in situ X-ray diffraction (XRD) heating experiment was performed on a sample of dried oleic acid modified NCs using a Panalytical X'Pert Pro MPD powder diffractometer equipped with a Cu source, a PIXcel detector, and an Anton-Paar XRK 900 reaction chamber. The measurements were performed under N_2 atmosphere. The sample was subsequently heated to 25, 150, 250, 325, 450, and again 25 °C with a heating rate of 10 K min^{-1} and an equilibration time of 1 h at each temperature step. The samples were scanned from 10–90° 2Θ with a step size of 0.01313° 2Θ and an integration time of 0.6 s per step.

Nanoindentation. Prior to nanoindentation, a portion of each sample (area of ca. 25 mm^2) was embedded in a cold curing acrylic mounting resin and polished down to a surface roughness of 50 nm using a sequence of SiC papers and diamond suspensions (for 15–0.25 μm from ATM GmbH, Germany, and for 0.05 μm from Buehler, Germany). To ensure that the embedding medium and substrate had no effect on the nanoindentation measurements, the thickness of the tested samples was at least 500 times larger than the indentation depth. The mechanical tests were performed in an Agilent Nano Indenter G200 (Agilent) system using the continuous stiffness measurement method, with a constant strain target of 0.05 s^{-1}, a harmonic displacement target of 2 nm, and a harmonic frequency of 45 Hz. The maximum indentation depth was set to 300 nm, based on a previous analysis on the indentation depth effects.[15] The system was equipped with a Berkovich tip. A number of 20 indents per sample was performed. The nanoindenter conducted the measurements in the displacement-control mode. After the desired indentation depth was reached, the load was held constant for 10 s before withdrawing the tip from the sample.

Ab Initio Molecular Dynamics Simulation. AIMD simulations were performed using the Vienna Ab Initio Simulation Package (vasp.5.4.4)[91] using the projector augmented wave method[92] and the Perdew–Burke–Ernzerhof generalized gradient approximation as the exchange–correlation functional.[93] The plane-wave cutoff was set to 250 eV and Gaussian smearing with a width of 0.1 eV, and a $1 \times 1 \times 1$ γ-centered k-point mesh was used. All simulations were run for 5000 fs using the Verlet integration algorithm. The temperature was set to 400 K in order to observe sufficient interactions during the simulation time, and the velocities were rescaled every 4 steps. The electronic self-consistency convergence condition was set to 10^{-5} eV. The mass of hydrogen atoms was changed to that of tritium to increase the time step to 1 fs.

ASSOCIATED CONTENT

Supporting Information

The Supporting Information is available free of charge at https://pubs.acs.org/doi/10.1021/acsnano.2c01332.

Starting suspension characterization; colloidal stability models; extended information on the self-assembled materials, compressed self-assembled materials and cross-linked SC materials under different atmospheres; further information on 3D model of interdigitating ligands and AIMD simulation; and data on in situ XRD under heat treatment (PDF)

AUTHOR INFORMATION

Corresponding Authors

Gerold A. Schneider – *Institute of Advanced Ceramics, Hamburg University of Technology, 21073 Hamburg, Germany*; orcid.org/0000-0001-5780-6249; Email: g.schneider@tuhh.de

Berta Domènech – *Institute of Advanced Ceramics, Hamburg University of Technology, 21073 Hamburg, Germany*; orcid.org/0000-0003-2042-4428; Email: berta.domenech@tuhh.de

Authors

Alexander Plunkett – *Institute of Advanced Ceramics, Hamburg University of Technology, 21073 Hamburg, Germany*; orcid.org/0000-0002-2356-113X

Michael Kampferbeck – *Institute of Physical Chemistry, University of Hamburg, 20146 Hamburg, Germany*; orcid.org/0000-0002-9657-5188

Büsra Bor – *Institute of Advanced Ceramics, Hamburg University of Technology, 21073 Hamburg, Germany*

Uta Sazama – *Institute of Inorganic and Applied Chemistry, University of Hamburg, 20146 Hamburg, Germany*

Tobias Krekeler – *Electron Microscopy Unit, Hamburg University of Technology, 21073 Hamburg, Germany*

Lieven Bekaert – *Research Group of Electrochemical and Surface Engineering, Vrije Universiteit Brussel, 1050 Brussels, Belgium*; orcid.org/0000-0003-1776-1888

Heshmat Noei – *Center for X-ray and Nano Science CXNS, Deutsches Elektronen-Synchrotron DESY, 22607 Hamburg, Germany*; orcid.org/0000-0003-1294-3527

Diletta Giuntini – *Institute of Advanced Ceramics, Hamburg University of Technology, 21073 Hamburg, Germany; Department of Mechanical Engineering, Eindhoven University of Technology, 5600 MB Eindhoven, The Netherlands*

Michael Fröba – *Institute of Inorganic and Applied Chemistry, University of Hamburg, 20146 Hamburg, Germany*; orcid.org/0000-0001-6927-0509

Andreas Stierle – *Center for X-ray and Nano Science CXNS, Deutsches Elektronen-Synchrotron DESY, 22607 Hamburg, Germany; Fachbreich Physik, University of Hamburg, 20355 Hamburg, Germany*; orcid.org/0000-0002-0303-6282

Horst Weller – *Institute of Physical Chemistry, University of Hamburg, 20146 Hamburg, Germany; Fraunhofer-CAN, 20146 Hamburg, Germany*; orcid.org/0000-0003-2967-6955

Tobias Vossmeyer – *Institute of Physical Chemistry, University of Hamburg, 20146 Hamburg, Germany*; orcid.org/0000-0001-9738-3826

Complete contact information is available at: https://pubs.acs.org/10.1021/acsnano.2c01332

https://doi.org/10.1021/acsnano.2c01332
ACS Nano 2022, 16, 11692–11707

Author Contributions

A.P. and B.D designed the study and wrote the manuscript. A.P, B.D., and M.K. performed the data analysis. M.K and T.V. performed the nanocrystal's surface functionalization and characterization (FTIR, EA, X-ray). A.P. and B.D. performed the supercrystalline materials preparation. A.P and B.D. performed the SAXS characterization. L.B., A.P, and B.D. performed the modeling and simulations. T.K, A.P, and B.D. performed the imaging (SAED, TEM, EDX, SEM). A.P. performed the TGA. U.S. performed the TGA-MS. B.B. performed the nanoindentation. H.N. performed the XPS. B.D and G.S. supervised the research. All authors discussed the results and coedited the manuscript.

Notes

The authors declare no competing financial interest.

ACKNOWLEDGMENTS

The authors gratefully acknowledge financial support from the Deutsche Forschungsgemeinschaft (DFG, German Research Foundation) project no. 192346071-SFB 986. B.B. gratefully acknowledges the support from the Ministry of National Education of the Republic of Turkey. The authors are very thankful to Emad Maawad (Deutsches Elektronen-Synchrotron, DESY) for his assistance in the SAXS acquisition, to Lea Klauke (Universität Hamburg) for her assistance in EA data acquisition, and to Vedran Vonk (DESY) for fruitful discussions about X-ray analyses.

REFERENCES

(1) Begley, M. R.; Gianola, D. S.; Ray, T. R. Bridging functional nanocomposites to robust macroscale devices. *Science (New York, N.Y.)* **2019**, *364*, No. eaav4299.

(2) Liu, J.; Huang, J.; Niu, W.; Tan, C.; Zhang, H. Unconventional-Phase Crystalline Materials Constructed from Multiscale Building Blocks. *Chem. Rev.* **2021**, *121*, 5830−5888.

(3) Li, Z.; Fan, Q.; Yin, Y. Colloidal Self-Assembly Approaches to Smart Nanostructured Materials. *Chem. Rev.* **2022**, *122*, 4976−5067.

(4) Bor, B.; Giuntini, D.; Domènech, B.; Plunkett, A.; Kampferbeck, M.; Vossmeyer, T.; Weller, H.; Scheider, I.; Schneider, G. A. Constitutive and fracture behavior of ultra-strong supercrystalline nanocomposites. *Applied Physics Reviews* **2021**, *8*, 031414.

(5) Domènech, B.; Tan, A. T. L.; Jelitto, H.; Zegarra Berodt, E.; Blankenburg, M.; Focke, O.; Cann, J.; Cem Tasan, C.; Colombi Ciacchi, L.; Müller, M.; Furlan, K. P.; John Hart, A.; Schneider, G. A. Strong Macroscale Supercrystalline Structures by 3D Printing Combined with Self−Assembly of Ceramic Functionalized Nanoparticles. *Adv. Eng. Mater.* **2020**, *22*, 2000352.

(6) Bian, K.; Li, R.; Fan, H. Controlled Self-Assembly and Tuning of Large PbS Nanoparticle Supercrystals. *Chem. Mater.* **2018**, *30*, 6788−6793.

(7) Wang, Z.; Singaravelu, A. S. S.; Dai, R.; Nian, Q.; Chawla, N.; Wang, R. Y. Ligand Crosslinking Boosts Thermal Transport in Colloidal Nanocrystal Solids. *Angewandte Chemie (International ed. in English)* **2020**, *59*, 9556−9563.

(8) Baranov, D.; Fieramosca, A.; Yang, R. X.; Polimeno, L.; Lerario, G.; Toso, S.; Giansante, C.; Giorgi, M. D.; Tan, L. Z.; Sanvitto, D.; et al. Aging of Self-Assembled Lead Halide Perovskite Nanocrystal Superlattices: Effects on Photoluminescence and Energy Transfer. *ACS Nano* **2021**, *15*, 650−664.

(9) Mueller, N. S.; Pfitzner, E.; Okamura, Y.; Gordeev, G.; Kusch, P.; Lange, H.; Heberle, J.; Schulz, F.; Reich, S. Surface-Enhanced Raman Scattering and Surface-Enhanced Infrared Absorption by Plasmon Polaritons in Three-Dimensional Nanoparticle Supercrystals. *ACS Nano* **2021**, *15*, 5523−5533.

(10) Wang, J.; Le-The, H.; Shui, L.; Bomer, J. G.; Jin, M.; Zhou, G.; Mulvaney, P.; Pinkse, P. W. H.; Berg, A.; Segerink, L. I.; et al. Multilevel Spherical Photonic Crystals with Controllable Structures and Structure−Enhanced Functionalities. *Advanced Optical Materials* **2020**, *8*, 1902164.

(11) Jiang, Z.; Pikul, J. H. Centimetre-scale crack-free self-assembly for ultra-high tensile strength metallic nanolattices. *Nature materials* **2021**, *20*, 1512−1518.

(12) Fratzl, P.; Weinkamer, R. Nature's hierarchical materials. *Prog. Mater. Sci.* **2007**, *52*, 1263−1334.

(13) Dreyer, A.; Feld, A.; Kornowski, A.; Yilmaz, E. D.; Noei, H.; Meyer, A.; Krekeler, T.; Jiao, C.; Stierle, A.; Abetz, V.; et al. Organically linked iron oxide nanoparticle supercrystals with exceptional isotropic mechanical properties. *Nature materials* **2016**, *15*, 522−528.

(14) Domènech, B.; Kampferbeck, M.; Larsson, E.; Krekeler, T.; Bor, B.; Giuntini, D.; Blankenburg, M.; Ritter, M.; Müller, M.; Vossmeyer, T.; et al. Hierarchical supercrystalline nanocomposites through the self-assembly of organically-modified ceramic nanoparticles. *Sci. Rep.* **2019**, *9*, 3435.

(15) Bor, B.; Giuntini, D.; Domènech, B.; Swain, M. V.; Schneider, G. A. Nanoindentation-based study of the mechanical behavior of bulk supercrystalline ceramic-organic nanocomposites. *Journal of the European Ceramic Society* **2019**, *39*, 3247−3256.

(16) Giuntini, D.; Torresani, E.; Chan, K. T.; Blankenburg, M.; Saviot, L.; Bor, B.; Domènech, B.; Shachar, M.; Müller, M.; Olevsky, E. A.; et al. Iron oxide-based nanostructured ceramics with tailored magnetic and mechanical properties: development of mechanically robust, bulk superparamagnetic materials. *Nanoscale Advances* **2019**, *1*, 3139−3150.

(17) Giuntini, D.; Zhao, S.; Krekeler, T.; Li, M.; Blankenburg, M.; Bor, B.; Schaan, G.; Domènech, B.; Müller, M.; Scheider, I. Defects and plasticity in ultrastrong supercrystalline nanocomposites. *Science advances* **2021**, *7*, abb6063 DOI: 10.1126/sciadv.abb6063.

(18) Giansante, C. Library Design of Ligands at the Surface of Colloidal Nanocrystals. *Accounts of chemical research* **2020**, *53*, 1458−1467.

(19) Winslow, S. W.; Swan, J. W.; Tisdale, W. A. The Importance of Unbound Ligand in Nanocrystal Superlattice Formation. *J. Am. Chem. Soc.* **2020**, *142*, 9675−9685.

(20) Weidman, M. C.; Nguyen, Q.; Smilgies, D.-M.; Tisdale, W. A. Impact of Size Dispersity, Ligand Coverage, and Ligand Length on the Structure of PbS Nanocrystal Superlattices. *Chem. Mater.* **2018**, *30*, 807−816.

(21) Guardia, P.; Batlle-Brugal, B.; Roca, A. G.; Iglesias, O.; Morales, M. P.; Serna, C. J.; Labarta, A.; Batlle, X. Surfactant effects in magnetite nanoparticles of controlled size. *J. Magn. Magn. Mater.* **2007**, *316*, e756−e759.

(22) Dadwal, A.; Joy, P. A. Influence of chain length of long-chain fatty acid surfactant on the thermal conductivity of magnetite nanofluids in a magnetic field. *Colloids Surf., A* **2018**, *555*, 525−531.

(23) Li, F.; Li, Y. C.; Wang, Z.; Li, J.; Nam, D.-H.; Lum, Y.; Luo, M.; Wang, X.; Ozden, A.; Hung, S.-F.; et al. Cooperative CO2-to-ethanol conversion via enriched intermediates at molecule−metal catalyst interfaces. *Nat. Catal.* **2020**, *3*, 75.

(24) Hosseini, S. N.; Grau-Carbonell, A.; Nikolaenkova, A. G.; Xie, X.; Chen, X.; Imhof, A.; Blaaderen, A.; Baesjou, P. J. Smectic Liquid Crystalline Titanium Dioxide Nanorods: Reducing Attractions by Optimizing Ligand Density. *Adv. Funct. Mater.* **2020**, *30*, 2005491.

(25) Winslow, S. W.; Liu, Y.; Swan, J. W.; Tisdale, W. A. Repulsive, Densely Packed Ligand-Shells Mediate Interactions between PbS Nanocrystals in Solution. *J. Phys. Chem. C* **2021**, *125*, 8014−8020.

(26) Fan, Z.; Grünwald, M. Orientational Order in Self-Assembled Nanocrystal Superlattices. *J. Am. Chem. Soc.* **2019**, *141*, 1980−1988.

(27) Schlotheuber né Brunner, J.; Maier, B.; Thomä, S. L. J.; Kirner, F.; Baburin, I. A.; Lapkin, D.; Rosenberg, R.; Sturm, S.; Assalauova, D.; Carnis, J.; et al. Morphogenesis of Magnetite Mesocrystals: Interplay between Nanoparticle Morphology and Solvation Shell. *Chem. Mater.* **2021**, *33*, 9119−9130.

(28) Kister, T.; Monego, D.; Mulvaney, P.; Widmer-Cooper, A.; Kraus, T. Colloidal Stability of Apolar Nanoparticles: The Role of

Particle Size and Ligand Shell Structure. *ACS Nano* **2018**, *12*, 5969−5977.
(29) Yun, H.; Lee, Y. J.; Xu, M.; Lee, D. C.; Stein, G. E.; Kim, B. J. Softness- and Size-Dependent Packing Symmetries of Polymer-Grafted Nanoparticles. *ACS Nano* **2020**, *14*, 9644−9651.
(30) Monego, D.; Kister, T.; Kirkwood, N.; Doblas, D.; Mulvaney, P.; Kraus, T.; Widmer-Cooper, A. When Like Destabilizes Like: Inverted Solvent Effects in Apolar Nanoparticle Dispersions. *ACS Nano* **2020**, *14*, 5278−5287.
(31) Arndt, B.; Sellschopp, K.; Creutzburg, M.; Grånäs, E.; Krausert, K.; Vonk, V.; Müller, S.; Noei, H.; Feldbauer, G. B. V.; Stierle, A. Carboxylic acid induced near-surface restructuring of a magnetite surface. *Communications Chemistry* **2019**, *2*, 92.
(32) Konuk, M.; Sellschopp, K.; Vonbun-Feldbauer, G. B.; Meißner, R. H. Modeling Charge Redistribution at Magnetite Interfaces in Empirical Force Fields. *J. Phys. Chem. C* **2021**, *125*, 4794−4805.
(33) Zhang, X.; Chen, L.; Yuan, L.; Liu, R.; Li, D.; Liu, X.; Ge, G. Conformation-Dependent Coordination of Carboxylic Acids with Fe3O4 Nanoparticles Studied by ATR-FTIR Spectral Deconvolution. *Langmuir: the ACS journal of surfaces and colloids* **2019**, *35*, 5770−5778.
(34) Zeng, J.; Jing, L.; Hou, Y.; Jiao, M.; Qiao, R.; Jia, Q.; Liu, C.; Fang, F.; Lei, H.; Gao, M. Anchoring group effects of surface ligands on magnetic properties of Fe_3 O_4 nanoparticles: towards high performance MRI contrast agents. *Adv. Mater.* **2014**, *26*, 2694−2698.
(35) Green, P. B.; Yarur Villanueva, F.; Imperiale, C. J.; Hasham, M.; Demmans, K. Z.; Burns, D. C.; Wilson, M. W. Directed Ligand Exchange on the Surface of PbS Nanocrystals: Implications for Incoherent Photon Conversion. *ACS Applied Nano Materials* **2021**, *4*, 5655−5664.
(36) Sauter, E.; Nascimbeni, G.; Trefz, D.; Ludwigs, S.; Zojer, E.; von Wrochem, F.; Zharnikov, M. A dithiocarbamate anchoring group as a flexible platform for interface engineering. *Physical chemistry chemical physics: PCCP* **2019**, *21*, 22511−22525.
(37) Sharifi Dehsari, H.; Harris, R. A.; Ribeiro, A. H.; Tremel, W.; Asadi, K. Optimizing the Binding Energy of the Surfactant to Iron Oxide Yields Truly Monodisperse Nanoparticles. *Langmuir: the ACS journal of surfaces and colloids* **2018**, *34*, 6582−6590.
(38) Wróbel, M.; Żaba, T.; Sauter, E.; Krawiec, M.; Sobczuk, J.; Terfort, A.; Zharnikov, M.; Cyganik, P. Thermally Stable and Highly Conductive SAMs on Ag Substrate—The Impact of the Anchoring Group. *Advanced Electronic Materials* **2021**, *7*, 2000947.
(39) Yu, S.; Kim, D.; Qi, Z.; Louisia, S.; Li, Y.; Somorjai, G. A.; Yang, P. Nanoparticle Assembly Induced Ligand Interactions for Enhanced Electrocatalytic CO2 Conversion. *J. Am. Chem. Soc.* **2021**, *143*, 19919−19927.
(40) Sahoo, Y.; Pizem, H.; Fried, T.; Golodnitsky, D.; Burstein, L.; Sukenik, C. N.; Markovich, G. Alkyl Phosphonate/Phosphate Coating on Magnetite Nanoparticles: A Comparison with Fatty Acids. *Langmuir: the ACS journal of surfaces and colloids* **2001**, *17*, 7907−7911.
(41) Ohno, T.; Kubicki, J. D. Adsorption of Organic Acids and Phosphate to an Iron (Oxyhydr)oxide Mineral: A Combined Experimental and Density Functional Theory Study. *J. Phys. Chem. A* **2020**, *124*, 3249−3260.
(42) Kreller, D. I.; Gibson, G.; Novak, W.; van Loon, G. W.; Horton, J. Competitive adsorption of phosphate and carboxylate with natural organic matter on hydrous iron oxides as investigated by chemical force microscopy. *Colloids Surf., A* **2003**, *212*, 249−264.
(43) Hanwell, M. D.; Curtis, D. E.; Lonie, D. C.; Vandermeersch, T.; Zurek, E.; Hutchison, G. R. Avogadro: an advanced semantic chemical editor, visualization, and analysis platform. *Journal of Cheminformatics* **2012**, *4*, 17.
(44) Derjaguin, B. Untersuchungen über die Reibung und Adhäsion, IV: Theorie des Anhaftens kleiner Teilchen. *Kolloid-Z.* **1934**, *69*, 155−164.
(45) Israelachvili, J. N. In *Intermolecular and Surface Forces*, 3rd ed.; Israelachvili, J. N., Ed.; Academic Press: Boston, 2011; pp 91−106.
(46) Evans, R.; Smitham, J. B.; Napper, D. H. Theoretical prediction of the elastic contribution to steric stabilization. *Colloid Polymer Sci.* **1977**, *255*, 161−167.
(47) Smitham, J. B.; Evans, R.; Napper, D. H. Analytical theories of the steric stabilization of colloidal dispersions. *Journal of the Chemical Society, Faraday Transactions 1: Physical Chemistry in Condensed Phases* **1975**, *71*, 285.
(48) Khan, S. J.; Pierce, F.; Sorensen, C. M.; Chakrabarti, A. Self-assembly of ligated gold nanoparticles: phenomenological modeling and computer simulations. *Langmuir: the ACS journal of surfaces and colloids* **2009**, *25*, 13861−13868.
(49) Goubet, N.; Richardi, J.; Albouy, P. A.; Pileni, M. P. How to Predict the Growth Mechanism of Supracrystals from Gold Nanocrystals. *J. Phys. Chem. Lett.* **2011**, *2*, 417−422.
(50) Håkonsen, V.; Singh, G.; Normile, P. S.; de Toro, J. A.; Wahlström, E.; He, J.; Zhang, Z. Magnetically Enhanced Mechanical Stability and Super−Size Effects in Self−Assembled Superstructures of Nanocubes. *Adv. Funct. Mater.* **2019**, *29*, 1904825.
(51) Wijenayaka, L. A.; Ivanov, M. R.; Cheatum, C. M.; Haes, A. J. Improved Parametrization for Extended Derjaguin, Landau, Verwey, and Overbeek Predictions of Functionalized Gold Nanosphere Stability. *J. Phys. Chem. C* **2015**, *119*, 10064−10075.
(52) Gerstner, D.; Kraus, T. Rapid nanoparticle self-assembly at elevated temperatures. *Nanoscale* **2018**, *10*, 8009−8013.
(53) Gao, A.; Liu, J.; Ye, L.; Schönecker, C.; Kappl, M.; Butt, H.-J.; Steffen, W. Control of Droplet Evaporation on Oil-Coated Surfaces for the Synthesis of Asymmetric Supraparticles. *Langmuir: the ACS journal of surfaces and colloids* **2019**, *35*, 14042−14048.
(54) Geva, N.; Shepherd, J. J.; Nienhaus, L.; Bawendi, M. G.; van Voorhis, T. Morphology of Passivating Organic Ligands around a Nanocrystal. *J. Phys. Chem. C* **2018**, *122*, 26267−26274.
(55) Lee, B.; Littrell, K.; Sha, Y.; Shevchenko, E. V. Revealing the Effects of the Non-solvent on the Ligand Shell of Nanoparticles and Their Crystallization. *J. Am. Chem. Soc.* **2019**, *141*, 16651.
(56) Dietrich, H.; Schmaltz, T.; Halik, M.; Zahn, D. Molecular dynamics simulations of phosphonic acid-aluminum oxide self-organization and their evolution into ordered monolayers. *Physical chemistry chemical physics: PCCP* **2017**, *19*, 5137−5144.
(57) Lokteva, I.; Koof, M.; Walther, M.; Grübel, G.; Lehmkühler, F. Coexistence of hcp and bct Phases during In Situ Superlattice Assembly from Faceted Colloidal Nanocrystals. *J. Phys. Chem. Lett.* **2019**, *10*, 6331−6338.
(58) Gu, X. W.; Ye, X.; Koshy, D. M.; Vachhani, S.; Hosemann, P.; Alivisatos, A. P. Tolerance to structural disorder and tunable mechanical behavior in self-assembled superlattices of polymer-grafted nanocrystals. *Proc. Natl. Acad. Sci. U.S.A.* **2017**, *114*, 2836−2841.
(59) Liu, X. P.; Ni, Y.; He, L. H. Elastic properties of gold supracrystals: Effects of nanocrystal size, ligand length, and nanocrystallinity. *J. Chem. Phys.* **2016**, *144*, 144507.
(60) Lee, J.; Wang, Z.; Zhang, J.; Yan, J.; Deng, T.; Zhao, Y.; Matyjaszewski, K.; Bockstaller, M. R. Molecular Parameters Governing the Elastic Properties of Brush Particle Films. *Macromolecules* **2020**, *53*, 1502−1513.
(61) Giuntini, D.; Davydok, A.; Blankenburg, M.; Domènech, B.; Bor, B.; Li, M.; Scheider, I.; Krywka, C.; Müller, M.; Schneider, G. A. Deformation Behavior of Cross-Linked Supercrystalline Nanocomposites: An in Situ SAXS/WAXS Study during Uniaxial Compression. *Nano Lett.* **2021**, *21*, 2891−2897.
(62) Jiao, Y.; Han, D.; Ding, Y.; Zhang, X.; Guo, G.; Hu, J.; Yang, D.; Dong, A. Fabrication of three-dimensionally interconnected nanoparticle superlattices and their lithium-ion storage properties. *Nat. Commun.* **2015**, *6*, 6420.
(63) Jiao, Y.; Han, D.; Liu, L.; Ji, L.; Guo, G.; Hu, J.; Yang, D.; Dong, A. Highly ordered mesoporous few-layer graphene frameworks enabled by fe3 o4 nanocrystal superlattices. *Angewandte Chemie (International ed. in English)* **2015**, *54*, 5727−5731.
(64) Yan, C.; Bor, B.; Plunkett, A.; Domènech, B.; Schneider, G. A.; Giuntini, D. Nanoindentation of Supercrystalline Nanocomposites:

https://doi.org/10.1021/acsnano.2c01332
ACS Nano 2022, 16, 11692−11707

Linear Relationship Between Elastic Modulus and Hardness. *JOM* **2022**, *74*, 2261.
(65) Schwarzenberg, A.; Ichou, F.; Cole, R. B.; Machuron-Mandard, X.; Junot, C.; Lesage, D.; Tabet, J.-C. Identification tree based on fragmentation rules for structure elucidation of organophosphorus esters by electrospray mass spectrometry. *Journal of mass spectrometry: JMS* **2013**, *48*, 576−586.
(66) Pretsch, E.; Bühlmann, P.; Affolter, C. *Structure Determination of Organic Compounds: Tables of Spectral Data*, 3rd ed.; Springer eBook Collection: Berlin, Heidelberg, 2000.
(67) Larquet, C.; Hourlier, D.; Nguyen, A.-M.; Torres-Pardo, A.; Gauzzi, A.; Sanchez, C.; Carenco, S. Thermal Stability of Oleate−Stabilized Gd 2 O 2 S Nanoplates in Inert and Oxidizing Atmospheres. *ChemNanoMat* **2019**, *5*, 539−546.
(68) Rudolph, M.; Erler, J.; Peuker, U. A. A TGA−FTIR perspective of fatty acid adsorbed on magnetite nanoparticles−Decomposition steps and magnetite reduction. *Colloids Surf., A* **2012**, *397*, 16−23.
(69) Daniel, P.; Shylin, S. I.; Lu, H.; Tahir, M. N.; Panthöfer, M.; Weidner, T.; Möller, A.; Ksenofontov, V.; Tremel, W. The surface chemistry of iron oxide nanocrystals: surface reduction of g-Fe2O3 to Fe3O4 by redox-active catechol surface ligands. *Journal of Materials Chemistry C* **2018**, *6*, 326−333.
(70) Blanksby, S. J.; Ellison, G. B. Bond Dissociation Energies of Organic Molecules. *Accounts of chemical research* **2003**, *36*, 255−263.
(71) Tallman, K. A.; Roschek, B.; Porter, N. A. Factors influencing the autoxidation of fatty acids: effect of olefin geometry of the nonconjugated diene. *J. Am. Chem. Soc.* **2004**, *126*, 9240−9247.
(72) Crnjar, E. D.; Witchwoot, A.; Nawar, W. W. Thermal oxidation of a series of saturated triacylglycerols. *Journal of agricultural and food chemistry* **1981**, *29*, 39−42.
(73) Nawar, W. W. Chemical changes in lipids produced by thermal processing. *J. Chem. Educ.* **1984**, *61*, 299.
(74) Rinaldi, L.; Wu, Z.; Giovando, S.; Bracco, M.; Crudo, D.; Bosco, V.; Cravotto, G. Oxidative polymerization of waste cooking oil with air under hydrodynamic cavitation. *Green Processing and Synthesis* **2017**, *6*, 25.
(75) Brodnitz, M. H. Autoxidation of saturated fatty acids. A review. *Journal of agricultural and food chemistry* **1968**, *16*, 994−999.
(76) Gardner, H. W. Oxygen radical chemistry of polyunsaturated fatty acids. *Free Radical Biol. Med.* **1989**, *7*, 65−86.
(77) Shahidi, F.; Zhong, Y. Lipid oxidation and improving the oxidative stability. *Chem. Soc. Rev.* **2010**, *39*, 4067−4079.
(78) Reis, A.; Spickett, C. M. Chemistry of phospholipid oxidation. *Biochimica et biophysica acta* **2012**, *1818*, 2374−2387.
(79) Akoh, C. C. *Food lipids: Chemistry, nutrition, and biotechnology*, 4th ed.; CRC Press Taylor & Francis Group: Boca Raton, FL, 2017.
(80) Minotti, G.; Aust, S. D. Redox cycling of iron and lipid peroxidation. *Lipids* **1992**, *27*, 219−226.
(81) Papuc, C.; Goran, G. V.; Predescu, C. N.; Nicorescu, V. Mechanisms of Oxidative Processes in Meat and Toxicity Induced by Postprandial Degradation Products: A Review. *Comprehensive Reviews in Food Science and Food Safety* **2017**, *16*, 96−123.
(82) Simic, M. G. Free radical mechanisms in autoxidation processes. *J. Chem. Educ.* **1981**, *58*, 125.
(83) *Quality in Frozen Food*; Erickson, M. C., Hung, Y.-C., Eds.; Springer: Boston, MA, 1997.
(84) *Semiconducting Metal Oxides for Gas Sensing*; Deng, Y., Ed.; Springer: Singapore, 2019.
(85) Liu, P.; Huo, M.; Shi, J. Nanocatalytic Medicine of Iron-Based Nanocatalysts. *CCS Chemistry* **2021**, *3*, 2445−2463.
(86) Ohloff, G. *Functional Properties of Fats in Foods*; Forster Publishing: Zurich, Switzerland, 1973.
(87) Bach, R. D.; Ayala, P. Y.; Schlegel, H. B. A Reassessment of the Bond Dissociation Energies of Peroxides. An ab Initio Study. *J. Am. Chem. Soc.* **1996**, *118*, 12758−12765.
(88) Nietzold, C.; Dietrich, P. M.; Ivanov-Pankov, S.; Lippitz, A.; Gross, T.; Weigel, W.; Unger, W. E. S. Functional group quantification on epoxy surfaces by chemical derivatization (CD)-XPS. *Surf. Interface Anal.* **2014**, *46*, 668−672.
(89) Domènech, B.; Plunkett, A.; Kampferbeck, M.; Blankenburg, M.; Bor, B.; Giuntini, D.; Krekeler, T.; Wagstaffe, M.; Noei, H.; Stierle, A.; et al. Modulating the Mechanical Properties of Supercrystalline Nanocomposite Materials via Solvent-Ligand Interactions. *Langmuir* **2019**, *35*, 13893−13903.
(90) Stierle, A.; Keller, T. F.; Noei, H.; Vonk, V.; Roehlsberger, R. DESY NanoLab. *JLSRF* **2016**, *2*, 140.
(91) Kresse, G.; Furthmüller, J. Efficient iterative schemes for ab initio total-energy calculations using a plane-wave basis set. *Physical review. B, Condensed matter* **1996**, *54*, 11169−11186.
(92) Blöchl, P. E. Projector augmented-wave method. *Physical review. B, Condensed matter* **1994**, *50*, 17953−17979.
(93) Perdew; Burke; Ernzerhof. Generalized Gradient Approximation Made Simple. *Physical review letters* **1996**, *77*, 3865−3868.

https://doi.org/10.1021/acsnano.2c01332
ACS Nano 2022, 16, 11692−11707